Developing Cuprous Oxide Thin Film Characterization Techniques to Illuminate Efficiency-Limiting Mechanisms in Photovoltaic Applications

by

Riley Eric Brandt

Submitted to the
Department of Mechanical Engineering
in Partial Fulfillment of the Requirements for the Degree of

Bachelor of Science

at the

Massachusetts Institute of Technology

June 2011

Signature of Author……
Department of Mechanical Engineering
May 16, 2011

Certified by……
Tonio Buonassisi
SMA Assistant Professor of Mechanical Engineering and Manufacturing
Thesis Supervisor

Accepted by……...
John H. Lienhard V
Collins Professor of Mechanical Engineering
Chairman, Undergraduate Thesis Committee

Developing Cuprous Oxide Thin Film Characterization Techniques to Illuminate Efficiency-Limiting Mechanisms in Photovoltaic Applications

by

Riley Eric Brandt

Submitted to the Department of Mechanical Engineering
on May 16, 2011, in partial fulfillment of the requirements for the degree of
Bachelor of Science in Mechanical Engineering

Abstract

Future fossil fuel scarcity and environmental degradation have demonstrated the need for renewable, low-carbon sources of energy to power an increasingly industrialized world. Solar energy, with its extraordinary resource base, is one of the most feasible long-term options for satisfying energy demand with minimal environmental impact. However, solar photovoltaic panels remain expensive and employ materials whose resource bases cannot satisfy global, terawatt-level penetration. This necessitates the development of cheap, earth-abundant semiconductors for solar conversion such as cuprous oxide (Cu_2O). Poor solar energy conversion efficiency (<2%) has hindered the development of this material, yet it is not well understood what is preventing the material from approaching the idealized maximum efficiency of 20%. The present work aims to develop a thorough characterization method for Cu_2O thin films fabricated through a physical vapor deposition (PVD) process known as reactive direct-current magnetron sputtering. This both provides a platform for material analysis and an opportunity to adapt a typically high-throughput manufacturing method to make high quality thin films. Spectrophotometry, Hall Effect mobility measurement, and photoelectrochemical cell techniques are used in succession to determine the absorption and transport properties. The films are found to have a direct forbidden bandgap of 1.93 eV, with an absorption coefficient of greater than 10^5 cm^{-1} for photons carrying energy in excess of 2.6 eV. Majority carrier mobility is measured as 58.1 $cm^2/V \cdot s$, approaching the levels of monocrystalline oxidized films in literature. These high mobilities indicate that with carrier lifetime >10 nanoseconds, minority carrier diffusion length could easily exceed the film thickness. The photoelectrochemical minority carrier diffusion length measurement achieves success on gallium arsenide test samples, determining flat-band potential, quantum efficiency, and minority carrier diffusion length, paving the way for future Cu_2O measurement. Future work may apply this test procedure to fully characterize other materials, and eventually lead to solar cell fabrication.

Thesis Supervisor: Tonio Buonassisi

Title: SMA Assistant Professor of Mechanical Engineering and Manufacturing

Acknowledgments

As a high school student deeply interested in applying technology to the major global issues of our time, the Massachusetts Institute of Technology was a natural choice. Yet at one point, the goal of attending and furthermore graduating from MIT seemed very far off. Between the reality now and that distant past lie a number of individuals that have made this journey possible.

Firstly, I must thank the incredible generosity of MIT and its community for providing me the opportunity to pursue my passions here. In particular I must thank the donors of the Audrey Stein Memorial and Class of 2001 Student Life Scholarship Funds, whose contributions provided me the means to achieve at MIT. Furthermore, I owe a great deal to the generosity of the Undergraduate Research Opportunities Program (UROP), whose funding enabled me to conduct the research that eventually led to the creation of this thesis.

Secondly, I wish to thank the many academic advisors that have provided me the tools to succeed in the sometimes overwhelming arena that is MIT. Most notably, I thank Professor John Brisson for his advice as an academic advisor, and Professor Carol Livermore for trusting me and for allowing me to prove to myself that I could handle academic research in my first ever UROP.

Thirdly, I wish to express a tremendous amount of gratitude to the individuals who directly advised me on my work with the Laboratory for Photovoltaics. Graduate students Yun Lee and Sin Cheng Siah provided both their extensive wisdom and extra pairs of hands to conduct experiments and achieve results. Most importantly though was the role of my advisor, Professor Tonio Buonassisi. Professor Buonassisi introduced me to the science of photovoltaics, then entertained my first research proposal and provided me the individuals and resources to pursue it. Since then, his optimism, wisdom, and oversight have consistently driven my work on this project.

Finally, and most importantly, I must thank my parents for their trust and support in the last four years and beyond. They were willing to accept a 17-year-old's dream of traveling hundreds of miles to start a new life at MIT, and ever since have provided endless motivation and reassurance. For getting me here, and helping me not only survive but thrive, I will never be able to thank them enough.

Contents

List of Figures

List of Tables

Nomenclature

Constants

c	= 2.998 x 10^{8} m·s^{-1}	Speed of light in free space
h	= 6.626 x 10^{-34} J·s	Planck Constant
k_B	= 1.381 x 10^{-23} J·K^{-1}	Boltzmann Constant
m_o	= 9.109 x 10^{-31} kg	Free electron mass
q	= 1.602 x 10^{-19} C	Elementary charge

Variables

α	Absorption coefficient [cm^{-1}]
C	Capacitance [F]
D	Diffusivity [$cm^2 \cdot s^{-1}$]
E	Energy [J], Electric Field Strength [$V \cdot cm^{-1}$]
Φ	Photon flux [s^{-1}]
G	Generation rate [$cm^{-3} \cdot s^{-1}$]
I	Intensity [$W \cdot cm^{-2}$]
J	Current density [$A \cdot cm^{-2}$]
k	Wave vector [m^{-1}]
L	Diffusion length [cm]
λ	Wavelength [nm]
m	Mass [kg]
m^*	Effective mass [kg]
μ	Mobility [$cm^2 \cdot V^{-1} \cdot s^{-1}$]
N	Number of states [1]
n	Index of Refraction [1], Concentration of electrons [cm^{-3}]
ν	Frequency [s^{-1}]
P	Probability [1]
p	Concentration of holes [cm^{-3}]
Q_F	Internal Quantum Efficiency [1]
R	Resistance [Ω]
ρ	Resistivity [Ω·cm]
σ	Conductivity [$\Omega^{-1} \cdot cm^{-1}$]
T	Temperature [K]
t	Film thickness [nm]
τ	Relaxation time, carrier lifetime [s]
V	Voltage [V]
W	Width [cm]
x	Distance [cm]

1. Introduction

1.1 Motivation

In 2010, civilization consumed over 500 exajoules of energy and in the process emitted over 30 billion metric tons of carbon dioxide [1]. It is difficult to comprehend such numbers – this energy consumption would be the equivalent of running 300 billion 50-watt light bulbs simultaneously for an entire year. As staggering as these numbers are, they are projected to grow. Annual global energy consumption may surpass 1000 exajoules in the next century given current trends [1]. As the inhabitants of non-OECD countries climb out of poverty and demand the lifestyles enjoyed by those in the developed world, resource consumption will grow accordingly. For individuals, this trend of higher energy consumption will enable upward mobility and, as it has done in the developed world, will make consumers wealthier and healthier with every additional unit of energy consumed.

To the collective, however, this disturbing trend represents the primary challenge of the 21st century. In a classic tragedy of the commons scenario, such massive resource consumption threatens civilization. By 2100 we may have exhausted our fossil fuel reserves, displaced hundreds of millions of people with rising sea levels, and spoiled our climate with desertification, pollution, and acidified oceans. Humanity's perpetual desire for increased prosperity and its means of attaining it are coming to a head, and thus the 21st century will require major changes to ensure long-term sustainability of civilization.

The change necessary to prevent catastrophic climate change is, quite simply, to reduce anthropogenic CO_2 emissions. A simplistic model describing net CO_2 emissions can be summarized in the following equation:

$$CO_2 = Population \times \frac{Energy}{Population} \times \frac{CO_2}{Energy}. \quad (1)$$

This identity breaks down the problem of CO_2 emissions into its underlying causes – growing population, increasing standard of living (energy per capita), and the carbon intensity of energy usage. Analyzing each term individually, it is clear the first two are difficult targets for addressing carbon dioxide emissions. The population problem has no technical or rapid solution, and as energy per capita is closely tied to prosperity, we expect this to rise inevitably with the growing affluence of the undeveloped world. We can, however, directly address the amount of CO_2 emitted per unit of energy consumed through technological innovation. This will require a transition to lower carbon sources of energy, consisting primarily of nuclear, geothermal, hydro, wind, and solar power.

Of all of these alternatives, solar represents perhaps the most promising long-term option. Whereas nuclear relies on an exhaustible fuel source with its own issues of waste production, and geothermal and hydro can only be deployed in a limited number of geographical areas, sun and wind power are accessible over much of the globe. Of the latter two technologies, solar offers a much larger resource base to capture. In fact, given an average solar flux of 1366 W/m^2, over 600 exajoules of solar energy (more than we currently consume in a year) strikes the earth's surface every hour. It is for these reasons that the author believes that solar energy is the necessary long-term solution to the energy and climate crises.

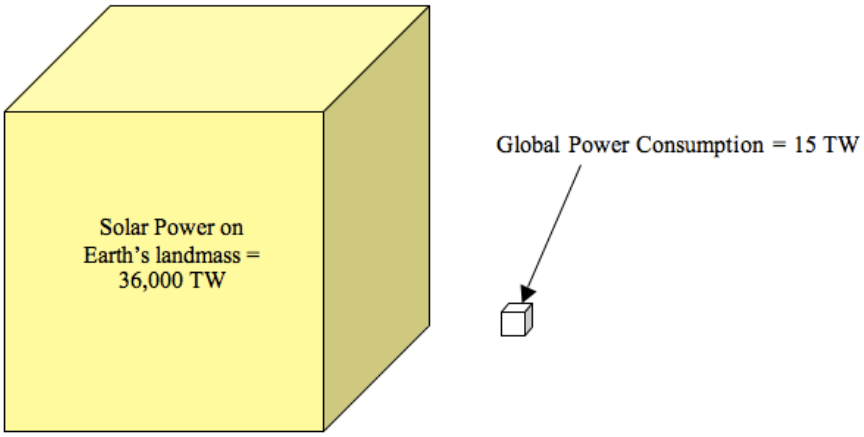

Figure 1-1: Available solar energy resource base compared to the current global energy demand.

However, the generation of useful energy from the sun's radiation still presents two critical challenges. Firstly, the cost of solar energy is still prohibitively expensive in most markets. Grid electricity sells for around 10-20 cents/kw·hr; and the cheapest sources such as coal can produce below this price. Table 1.1 provides an Energy Information Administration (EIA) comparison of the cost of current technologies, with fossil fuels in the 9-14 ¢/kw·hr range and photovoltaics just over 30 ¢/kw·hr [2].

Table 1.1: Estimated Levelized Cost of New Generation Resources, 2016 [2]

Plant Type	Capacity Factor (%)	U.S. Average Levelized Costs (2009 $/megawatthour) for Plants Entering Service in 2016				
		Levelized Capital Cost	Fixed O&M	Variable O&M (including fuel)	Transmission Investment	Total System Levelized Cost
Conventional Coal	85	65.3	3.9	24.3	1.2	94.8
Advanced Coal	85	74.6	7.9	25.7	1.2	109.4
Advanced Coal with CCS	85	92.7	9.2	33.1	1.2	136.2
Natural Gas-fired						
Conventional Combined Cycle	87	17.5	1.9	45.6	1.2	66.1
Advanced Combined Cycle	87	17.9	1.9	42.1	1.2	63.1
Advanced CC with CCS	87	34.6	3.9	49.6	1.2	89.3
Conventional Combustion Turbine	30	45.8	3.7	71.5	3.5	124.5
Advanced Combustion Turbine	30	31.6	5.5	62.9	3.5	103.5
Advanced Nuclear	90	90.1	11.1	11.7	1.0	113.9
Wind	34	83.9	9.6	0.0	3.5	97.0
Wind – Offshore	34	209.3	28.1	0.0	5.9	243.2
Solar PV[1]	25	194.6	12.1	0.0	4.0	210.7
Solar Thermal	18	259.4	46.6	0.0	5.8	311.8
Geothermal	92	79.3	11.9	9.5	1.0	101.7
Biomass	83	55.3	13.7	42.3	1.3	112.5
Hydro	52	74.5	3.8	6.3	1.9	86.4

[1] Costs are expressed in terms of net AC power available to the grid for the installed capacity.

To attain a competitive levelized cost of electricity over the lifetime of the plant, a commonly accepted metric is that the solar panels must cost below $1 per peak watt produced. In other words, a 1 m^2 panel rated at 100 W under a peak solar spectrum (1000W/m^2 of intensity) must cost no more than $100 to purchase and install for it to compete with grid electricity rates over its lifetime. This is the holy grail of photovoltaic research known as "grid parity" – where the levelized cost of producing electricity from the sun drops below market electricity rates and therefore becomes economically viable without subsidies. Fig. 1-2 demonstrates how close current technologies are to achieving this in sunny climates with higher market electricity rates.

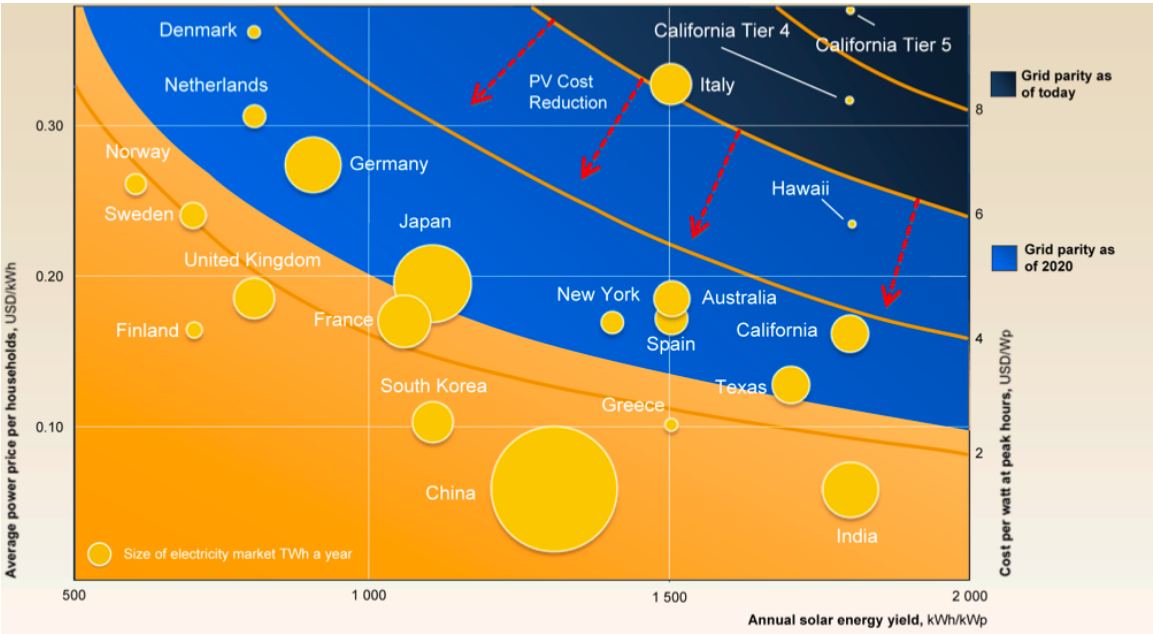

Figure 1-2: From McKinsey report on solar competitiveness, comparing the dollar-per-peak-watt price of solar panels with potential locations for installation, based on local electricity prices and the availability of the solar resource. The horizontal axis compares the annual solar yield, the left axis indicates retail electricity rates, and the curved lines at right indicate grid parity at different installed prices in $/$W_p$ [3].

With the least expensive plants installing solar panels for $6/$W_p$, solar is already surpassing grid parity in markets with high solar yield and high grid electricity rates. It will take a significant reduction in cost, however, to reach global grid parity and penetrate the larger electricity markets in the US, China, and much of the industrializing world.

The second barrier to widespread photovoltaic deployment is the availability of materials. Currently, photovoltaic modules make up a very small percentage of the world's energy base, at less than 0.1% [2]. To produce hundreds of exajoules of electricity, solar panels will need to be manufactured at the scale of more ubiquitous products such as automobiles or plastic bottles. At this scale, the materials involved in production become a major limiting factor. Materials such as tellurium, gallium, or indium used in modern solar cells are rare, and will never scale to cover the many square miles necessary to power the world with solar. Even ignoring the obvious problem of insufficient supply, using a scarce material presents a crippling economic paradox.

Proponents of solar energy expect solar cells to achieve increasing returns to scale, such that the cost of producing cells drops as processes are refined and high-throughput factories are built. Yet, the economics of scarce resources suggest that as demand for a material increases and supply remains fixed, the price will grow prohibitively instead.

There are two important steps that the photovoltaic industry can take in addressing the material constraint, and in turn the cost constraint. The first is to move towards thin film solar cells, requiring significantly less absorber material than industry standard silicon-based cells. The second is to use earth abundant materials in place of the more rare semiconductors that are researched today. There has been increasing attention placed on this field of earth abundant thin-film solar cells recently, as solar advocates realize the need to plan for terawatt-level capacity in the future [4].

Surveying all of the possible semiconductors available for solar applications, it is possible to classify them by the quantity of material reserves and the cost of the material to predict which would be the most scalable candidates, as seen in Fig. 1-3.

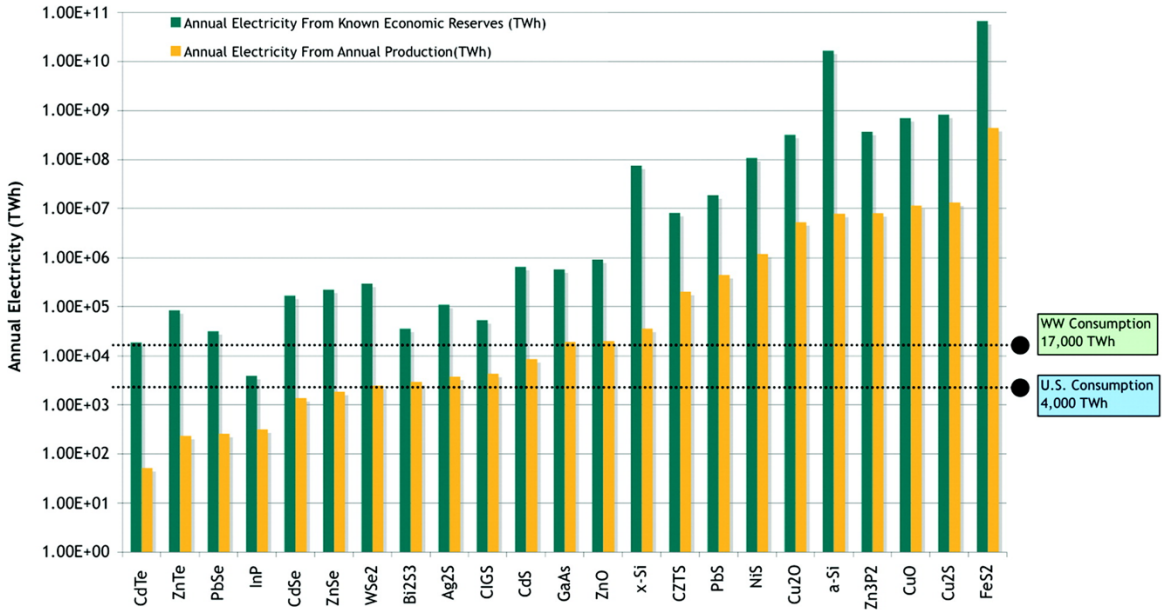

Figure 1-3: Estimated material requirements for 22 semiconductors to achieve worldwide electricity output as compared to available production and reserves of these materials, emphasizing importance of relative abundance [4]

One of the most promising options is cuprous oxide (Cu_2O), a group II-VI semiconductor with a cubic lattice arrangement of oxygen and monovalent copper atoms. Oxygen is the most abundant element on earth, and copper, while not as common in the earth's crust, claims an extensive mining operation that already produces over 16 million tons of copper annually [5]. The promise of cuprous oxide is therefore its low cost and high availability. If a Cu_2O solar cell could reach grid parity in mass production, it could rapidly scale to satisfy humanity's 1000 exajoule energy demand all over the globe.

1.2 Problem Statement

The promise of Cu_2O as a photovoltaic material has not gone unnoticed. The earliest publication suggesting the viability of a Cu_2O solar cell dates from 1960 [6]. In

the years since this publication, silicon has become the dominant solar cell material, while no successful Cu_2O cell has ever been produced. This is due in large part to the poor performance of existing devices – the maximum published efficiency of a solar cell fabricated from Cu_2O is 2.0% [7]. This figure is far from the potential performance of an ideal Cu_2O cell.

A commonly used metric for evaluating the maximum potential of a solar cell is the Shockley-Queisser efficiency limit [8]. This calculation compares the energy of incoming solar photons with the minimum photon energy required to generate current in a solar cell, also known as the bandgap of the semiconductor. If the bandgap is too high, lower energy photons cannot be absorbed at all, and go to waste. On the other hand, if the bandgap is too low, higher energy photons will only donate a small fraction of their energy to generating electricity. We can therefore predict what the maximum efficiency of a solar cell would be given the spread of photon energies the sun emits. Fig. 1-4 displays the maximum efficiency expected at each bandgap based on this spectrum.

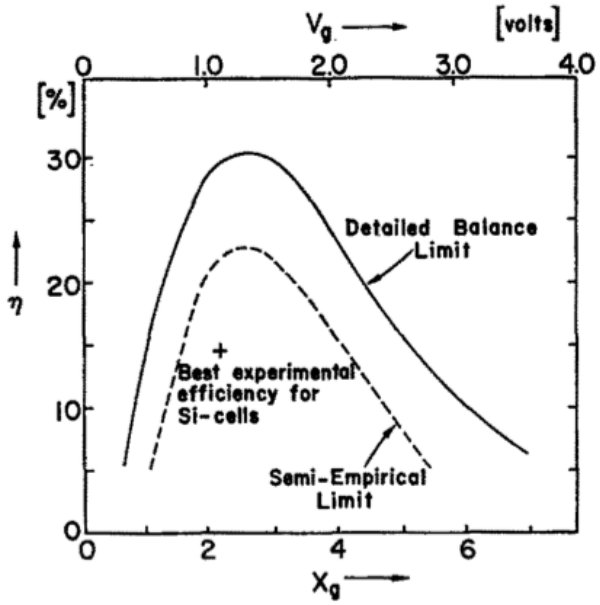

Figure 1-4: The predicted maximum efficiency of a single-junction solar cell in AM0 sunlight, as a function of the bandgap of the semiconductor [8].

Cuprous oxide is known to have a bandgap of roughly 2.0 electron volts (eV), which corresponds to a maximum theoretical efficiency of 20%. Silicon solar cells with a maximum theoretical efficiency of 32% have reached over 25% in practice, proving that it is possible to approach the maximum, ideal efficiency with improvements in material quality and cell architecture. This is a promising sign for cuprous oxide, as it suggests that such a cell could achieve efficiencies much higher than the current best-published 2% figure.

This raises the question, what is limiting Cu_2O cell efficiency? Fundamentally, what is preventing the consistent conversion of incoming photons to usable electricity?

In general, problems can arise in the generation, transport, and separation of electric carriers in a cell. With respect to carrier generation, a semiconductor could be a poor absorber. Crystalline silicon, for example, with an indirect bandgap, requires a semiconducting layer two orders of magnitude greater than thin film materials (e.g.

cadmium telluride) because of its poor absorption. However, Cu_2O is a direct bandgap semiconductor with strong absorption (an absorption coefficient of over 10^5 cm^{-1} for >2.6eV energy photons in the present work), suggesting that given proper antireflective cell design, a Cu_2O thin film cell would have no problem generating carriers.

With respect to carrier separation, this is primarily an issue of proper junction and module engineering. Cu_2O, however, does exhibit a very high exciton binding energy of approximately 150 meV [9]. This means that for incoming photons with energy just above the bandgap, electrons and holes may not be distinctly formed and will instead form an exciton pair that is much more difficult to separate.

This leaves carrier transport, the most likely candidate affecting Cu_2O performance. One can summarize the properties of how rapidly carriers like electrons diffuse through a semiconductor and how often they recombine, or relax down to a non-useful energy state before being extracted, with one metric – the minority carrier diffusion length. This describes the average length that we may expect a minority carrier (e.g. an electron in a p-type semiconductor) to travel before recombining with a carrier of opposite charge. To extract the carriers generated by incoming radiation, they must have a diffusion length on the order of the thickness of the device. If the diffusion length is too short, many of the carriers will recombine or go to waste before being extracted and used in an external circuit.

1.3 Aims and Objectives

In light of the above discussion, it is clear how critical it is to better understand the semiconducting properties of Cu_2O. As the most likely reason for poor efficiency is poor transport properties, it is particularly important to look at the transport properties of the Cu_2O thin films produced in our lab.

Thus, the aim of the present work is to build upon two important research efforts in the Laboratory for Photovoltaics at MIT. Firstly, we have developed an improved physical vapor deposition method using high-temperature annealing to deposit high quality p-type Cu_2O films; and secondly, we have begun characterizing these films to compare to existing literature. The purpose of the present work is to review and develop a procedure for measuring absorption, majority carrier mobility, and minority carrier diffusion length of thin film semiconductors. It is hoped that formulating these techniques will lay the groundwork for fully understanding Cu_2O. This understanding will both help determine what exactly is limiting cell efficiency, and provide a clear direction for how material improvements might help solve the problem of poor performance.

2. Physics

2.1 Photovoltaic Cell Basics

Photovoltaic (PV) cells are devices that convert the electromagnetic energy carried by light into electrical energy. First conceived in 1839 by Alexandre-Edmond Becquerel, it would take over a century before scientists could engineer the materials necessary to build a highly efficient solar cell. This section seeks to describe the basic principles of a solar cell, and the effect of certain material properties on the cell's performance.

The sun, formed at the birth of the solar system 4.6 billion years ago, is the primary source of energy for life on this planet. Inside the dense center of the sun, gravitational force and high temperatures force hydrogen molecules to undergo fusion, forming higher mass elements and releasing tremendous amounts of nuclear energy in the process. This positive feedback loop helps drive the sun's temperature higher and instigate further fusion reactions, resulting in temperatures of 13.6 million Kelvin (K) in the core and approximately 5800 K at the surface. As the molecules that make up the sun's mass reach such high temperatures, they vibrate with a tremendous amount of kinetic energy and emit this energy in the form of electromagnetic radiation. This radiation travels in all directions, illuminating earth and donating its energy to the life contained here. The primary mechanism for this energy conversion is photosynthesis, where plant matter absorbs particles of light energy, called photons, to do work and drive chemical reactions within the plant.

Solar cells, an inorganic corollary to photosynthesis, allow for the conversion of the sun's electromagnetic energy into usable electricity. Incoming photons excite electrons in the cell's absorbing material, a semiconductor, giving them enough energy to conduct. These excited electrons leave behind a hole, a positively charged "particle" akin to a bubble of air in water. The electrons and holes diffuse separately through the material until they reach a junction, usually formed at the interface of two different semiconducting materials. The electric field at the junction causes the negatively charged electron to move in one direction and the positively charged hole to move in the other direction, and the only way they may recombine is by traveling through an external circuit. A free, conducting electron traveling through a circuit is the basis for electricity. Thus, by generating free carriers (electrons and holes) and extracting them out of the cell, they may do useful work in the same way that a battery would supply such free carriers to power a light bulb, motor, or any other electrical device.

This general picture of how a solar cell converts electromagnetic energy (photons) into electrical energy (electrons and holes) gives us a simple model for understanding the performance of a solar cell. This performance depends on three primary steps - the ability to generate free electrons and holes from photons, the ability of those photogenerated carriers to travel through the cell, and finally, the ability to separate and extract those carriers from the cell. In improving the performance at each step, one can create a highly efficient solar panel that produces the maximum possible electricity. The following sections will discuss in more detail how each physical process works, thereby illuminating the potential limiting factors.

2.2 Optical Absorption

Understanding how photons interact with a solid semiconducting material is a critical part of understanding how photovoltaic cells work. To understand absorption, however, one must first understand the atomic structure of a semiconductor and the physics of light.

2.2.1 Electromagnetic Radiation

As Bohr first postulated in 1913, atoms consist of a dense, positively charged nucleus surrounded by a cloud of negatively charged electrons. These electrons, according to Bohr's quantum mechanics, can only exist in very specific "quantized"

energy levels, or orbits. Each orbit corresponds to a certain amount of energy, and thus to move between orbit levels the electron must absorb or release energy. The most common form of energy transfer is the photon – a quantum particle or wave containing electromagnetic energy equivalent to the frequency at which the wave vibrates, ν, multiplied by the Planck Constant, $h = 6.626 \times 10^{-34}$ J·s such that

$$E_{photon} = h\nu. \tag{2}$$

Photons may be modeled as either a particle or a wave, and both interpretations are of use in the current work. As a wave, light can be characterized by its temporal frequency ν and spatial wavelength λ. In free space, the relationship between how often the wave oscillates and how far it travels in one oscillation determines the speed of light,

$$c = \lambda\nu. \tag{3}$$

Thus, photons of light, while always traveling at the same speed, may oscillate at any frequency and carry any amount of energy. Electromagnetic radiation is therefore naturally represented by a spectrum, as illustrated in Fig. 2-1. Photons oscillating at high frequencies contain higher energy (kilo-electron volts) but shorter wavelengths (picometers), while lower frequency photons contain much smaller energies (milli-electron volts) and longer wavelengths (kilometers). Between these two extremes lies the visible region, at wavelengths from 380-740nm. Human eyes have evolved to perceive this small subsection of the electromagnetic spectrum because the sun emits most intensely in this region. By evolutionary coincidence, the part of the spectrum that we perceive through sight is also the most relevant region for producing electricity from the sun.

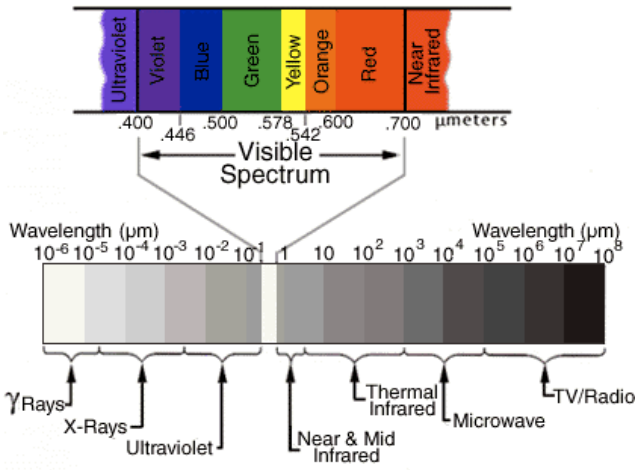

Figure 2-1: The EM spectrum, with visible wavelengths from 380-740nm [10].

The region of the electromagnetic spectrum over which the sun emits is defined by a property known as blackbody radiation. A blackbody is a substance with 100% emissivity and absorptivity – in other words, all incident photons are fully absorbed. Over the visible spectrum, such a material would appear jet black as no incident light is scattered backwards, giving rise to the name "blackbody". At the surface of the sun, lightweight hydrogen molecules vibrate with high kinetic energy, as the surface temperature averages 5800 K. The acceleration of electric charge creates a sinusoidal time-varying electric field, in turn generating a time-varying magnetic field, and it is this coupled field that forms a photon.

However, what we perceive as temperature is in reality an average of kinetic energy over many molecules. While 5800K corresponds with a kinetic energy of 0.5 electron volts (eV), the atoms at the surface of the sun contain a wide spread of kinetic energies. In turn, the atoms vibrate and emit over a wide range of frequencies. The range of frequencies emitted can be characterized by Planck's Law, expressed here as the emitted power per unit area, per unit solid angle, per unit frequency:

$$I(\nu) = \frac{2h\nu^3}{c^2}\left(\frac{1}{e^{\frac{h\nu}{k_B T}} - 1}\right). \tag{4}$$

Alternatively, Planck's Law may be expressed as a function of wavelength:

$$I(\lambda) = \frac{2hc^2}{\lambda^5}\left(\frac{1}{e^{\frac{hc}{\lambda k_B T}} - 1}\right). \tag{5}$$

Given the sun's surface temperature of 5800 K and the solid angle tended by the Earth, the solar spectrum may be determined from this equation, as seen in Fig. 2-2.

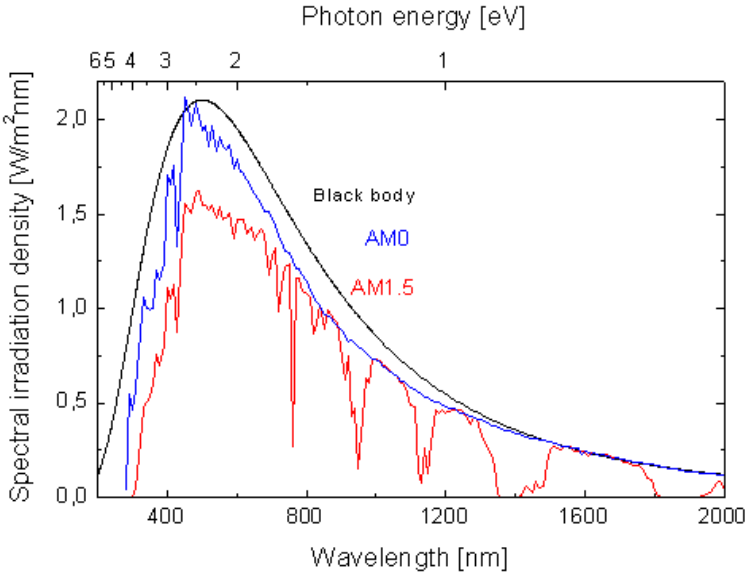

Figure 2-2: The solar spectrum displaying energy flux at each wavelength. The graph displays the difference between the ideal spectrum and what is actually observed as a result of attenuation. [11]

As seen in Fig. 2-2, the actual spectrum observed at the earth's surface differs from the ideal blackbody spectrum predicted, for two reasons. Firstly, the surface of the sun is not an ideal blackbody emitter as the temperature can vary substantially, radiation is absorbed and re-emitted, and sporadic flares allow for significant variation in emissions. Furthermore, the 100 kilometers of atmosphere through which incoming radiation must travel tends to absorb a fraction of the electromagnetic energy. Water vapor and ozone in particular cause scattering across a wide number of wavelengths, most noticeably reducing the intensity of higher energy ultraviolet (below 380nm wavelength) radiation. Some molecules like CO_2 and water vapor are also strongly absorptive over specific bands of the spectrum, corresponding to natural resonant frequencies for these molecules.

To capture the affect of the atmosphere on solar radiation ("insolation") intensity, we can characterize the flux on a solar panel by the amount of atmosphere it must travel through. Air-mass 0, or AM0 insolation describes the solar spectrum before entering the atmosphere, as a satellite orbiting Earth might encounter. Air-mass 1, or AM1, describes the distance the insolation must travel through the atmosphere directly perpendicular to the earth's surface, or the minimum distance possible. The most commonly used spectrum is the AM1.5, which represents an atmosphere thickness 1.5 times the minimum, or what a panel might receive from the sun at a 48.2° angle from normal. As the sun's angle (and therefore atmospheric distance it must travel through) varies according to time of day and latitude, the AM1.5 spectrum is a common standard.

In summary, the sun emits a broad spectrum of photons of many different wavelengths and energies. This spectrum is determined by the temperature distribution at the surface of the sun, and has a peak intensity at 520 nm or 2.4 eV. This solar spectrum strikes the earth with a power flux of 1366 W/m^2 before entering the atmosphere. The atmosphere then attenuates the intensity by absorbing or scattering some photons, resulting in a modified spectrum striking a solar panel at ground level. These photons are then absorbed by the solar panel to produce useful electricity.

2.2.2 Semiconductor Band Structure

Bohr's atomic model describing quantized, specific energy levels for each electron is effective only for single atoms. It does not explain the structure of atoms when assembled in a solid. As trillions of atoms are forced together in a crystal lattice, their interatomic spacing becomes so small that the electron clouds of neighboring atoms begin to overlap. In metals, the electrons effectively become a single cloud throughout the material, and can move around freely between atoms. This phenomenon gives rise to a metal's high conductivity.

Semiconductors, as their name suggests, form a more complicated electronic structure. As the atoms get closer, the many electron levels in the individual atoms merge to form two specific energy bands. Fig. 2-3 demonstrates how many s, p, d, or f electron orbitals can join to form two distinct energy levels – a valence and conduction band.

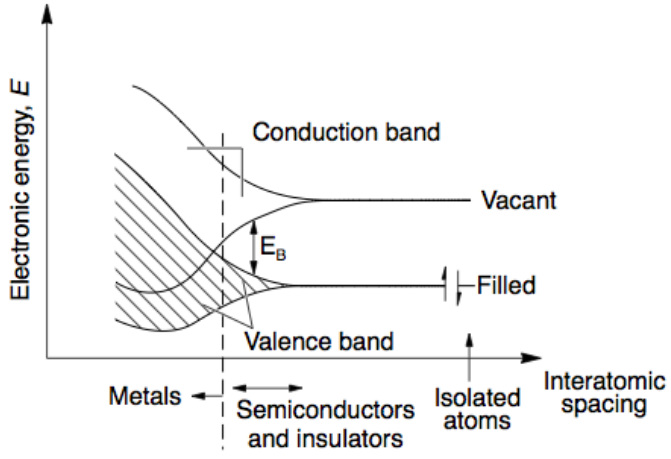

Figure 2-3: Small interatomic spacing leads the individual orbital levels to split and form different electron energy structure as seen here. At a certain interatomic distance those levels can be defined as two energy bands [12].

The lower energy grouping is referred to as the valence band (where electrons are less mobile), while the higher energy band is referred to as the conduction band (where electrons are free to move throughout the solid). In a pure semiconductor, no electrons can inhabit the energy levels in between these two bands. This forbidden region is known as the bandgap. It is important to recognize that the valence and conduction levels do not represent single energy levels for electrons and holes, but rather represent the boundaries of acceptable electron and hole energy states.

At temperatures of 0 K, all electrons inhabit the valence band in a semiconductor, reducing conductivity to zero. However, as the temperature rises, electrons in the valence band can achieve high enough thermal energy to be thermally excited into the conduction band. The temperatures need not be substantial – at room temperature, where the average kinetic energy is 26 meV, a small fraction of electrons obtain enough energy to jump bandgaps two orders of magnitude greater. As the temperature rises further, more electrons can move into the conduction band (leaving holes behind in the valence band), which enables higher conductivity in the semiconductor.

2.2.3 Absorption

Solar cell operation, however, relies on a more direct form of energy transfer between valence and conduction bands: the photogeneration of carriers. As discussed previously, each photon carries with it a specific amount of energy. If a photon's energy exceeds the difference in energy between the valence and conduction bands, the photon can be absorbed by an electron in the valence band and will be promoted into the conduction band. Fig. 2-4 demonstrates this phenomenon of photo-excitation pictorially. Note that the larger the bandgap, the less likely it is that carriers can move into the conduction band. These materials form a familiar class known as insulators, incapable of electrical conductivity due to the lack of charge carriers populating the conduction band.

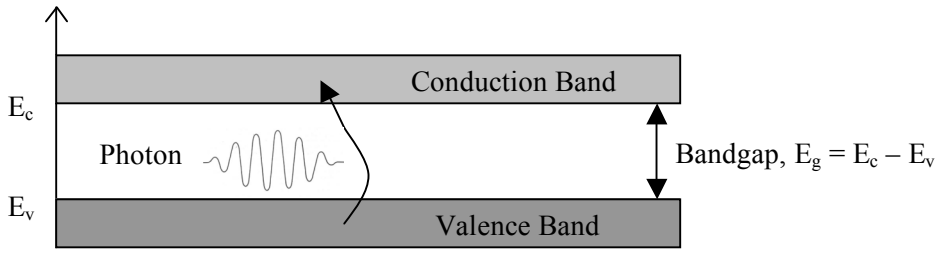

Figure 2-4: A valence band electron absorbing a photon's energy and being excited into the conduction band, if $E_{photon} > E_g$.

Photons with energy in excess of the bandgap are readily absorbed, as they are likely to have enough energy to excite electrons that are not right up against the band edge. However, for photons just above the bandgap, the thermal spread of carriers away from the band edges may prevent carrier excitation. Thus, we expect absorption to grow exponentially as a function of photon energy above the bandgap. This absorption strength is quantified with the absorption coefficient α [cm^{-1}]. The intensity $I(x)$ of incoming radiation in watts is attenuated in the material according to this absorption coefficient and the distance traveled such that

$$I(x) = I_O e^{-\alpha x}. \tag{6}$$

Lower energy photons, with a lower probability of absorption, must on average travel a further distance through the material before being absorbed; hence they would have a smaller absorption coefficient.

The absorption coefficient provides a highly effective way of characterizing the likelihood of free charge carriers to be excited into the conduction band, as a function of the incoming photon energy. This coefficient, however, varies substantially depending on whether the cell has a direct or indirect bandgap. A direct bandgap indicates that the minimum distance between valence and conduction energy bands occurs at a single momentum. Thus, the electron may absorb the photon and directly jump into the conduction band with no change in momentum. However, in an indirect bandgap semiconductor, the valence band energy peak and conduction band energy minimum occur at two different momentums. Thus, the electrons must undergo a change in momentum in addition to photon absorption in order to be fully excited into the conduction band. Fig. 2-5 displays this difference pictorially.

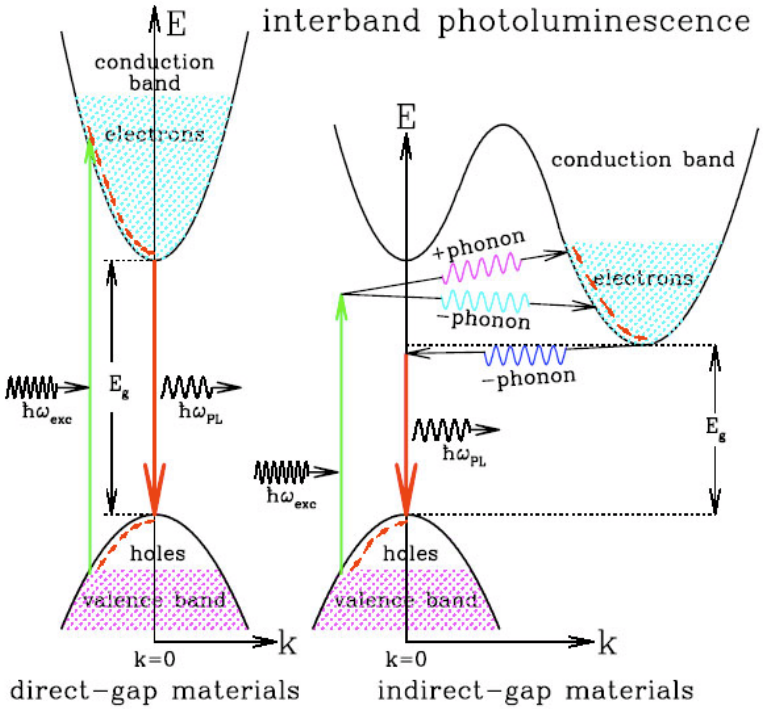

Figure 2-5: Direct vs. indirect bandgaps, with momentum on the abscissa and energy on the ordinate. Both require the same energy transfer for a carrier to move between bands, however in the indirect case, an additional momentum transfer must occur [13].

J. Bardeen, F. J. Blatt, and L. H. Hall have derived an extensive model to describe how the absorption coefficient may vary as a function of photon energy for different energy band transitions [14]. Their theory pertains specifically to absorption near the band edge, or for photons with energies on the order of the bandgap of the semiconductor. We assume first that photons carry a negligible amount of momentum such that momentum transfer only occurs through phonons, or lattice vibrations. Furthermore, we assume that the absorption coefficient for a particular energy of photon is proportional to the probability of transition from initial to final state P_{if}, proportional to

the densities of electrons in initial state, n_i, and proportional to the density of empty final states, n_f. Summing this up over all possible transitions of energy equal to $h\nu$:

$$\alpha(h\nu) = A\sum P_{ij} n_i n_f . \tag{7}$$

For the purposes of these derivations, we make the additional assumption that the semiconductor is undoped and at 0 K, specifically entailing that all valence states are filled and all conduction band states are initially empty.

For direct band-to-band transitions, no momentum transfer occurs; there is a single transition for which the probability is independent of momentum. Each initial energy level E_i on the valence band maps directly to a final energy level E_f on the conduction band, related by the photon energy such that

$$E_f = h\nu - E_i . \tag{8}$$

The bands are approximated as parabolic as in Fig. 2-5, thus if we take E_v to indicate the maximum energy of the valence band and E_c to be the minimum energy of the conduction band, we can describe the energy-momentum relationship for the valence and conduction bands respectively as:

$$E_v - E_i = \frac{\hbar^2 k^2}{2m_e^*}, \tag{9}$$

$$E_f - E_c = \frac{\hbar^2 k^2}{2m_h^*}. \tag{10}$$

Here, $\hbar = h/2\pi$, k is momentum (wave vector), and m_e^* and m_h^* are the effective masses of the electrons and holes respectively. This produces a relationship between the wave vector and the energy a photon must have in excess of the bandgap (E_g):

$$h\nu - E_g = \frac{\hbar^2 k^2}{2}\left(\frac{1}{m_e^*} + \frac{1}{m_h^*}\right). \tag{11}$$

The three dimensional density of states for fermions like electrons and holes can be defined as

$$N(h\nu)d(h\nu) = \frac{8\pi k^2 dk}{(2\pi)^3}, \tag{12}$$

which describes the number of states available at each wave vector k. Combining equations (11) and (12), we obtain an expression for the absorption coefficient as a function of photon energy:

$$\alpha(h\nu) = \frac{q^2\left(\frac{2}{m_e^*} + \frac{2}{m_h^*}\right)^{3/2}}{nch^2 m_e^*}(h\nu - E_G)^{1/2} . \tag{13}$$

$$\therefore \alpha(h\nu) \propto (h\nu - E_G)^{1/2}$$

In summary, the absorption coefficient for direct transitions at the band edge is, to first order, proportional to the energy in excess of the bandgap, to the $^1/_2$ power. This relationship is very useful for modeling basic direct transitions and for determining the bandgap of a material from its absorptive properties, but it only describes direct band-to-band transitions.

In addition, it is possible to have forbidden direct transitions as a result of quantum selection rules [14]. Here, transitions at k=0 are forbidden, and the transition

probability scales with k^2 elsewhere. For these transitions, due to the additional k^2 factor, the absorption coefficient is instead:

$$\alpha(h\nu) \propto (h\nu - E_G)^{3/2}. \tag{14}$$

Indirect transitions are more difficult to model, as they require an additional momentum transfer in the form of a phonon. This phonon must contain a certain momentum corresponding to the difference in band edges, and additionally contains energy E_{ph}. As a phonon may be emitted or absorbed during the transition, there are two possible energy transitions that may occur:

$$\begin{cases} h\nu = E_f - E_i + E_{ph} \\ h\nu = E_f - E_i - E_{ph} \end{cases}. \tag{15}$$

Additionally, the density of initial and final energy states can be modeled as in the direct case as, respectively

$$N(E_i) = \frac{1}{2\pi^2\hbar^2}(2m_h^*)^{3/2}(E_v - E_i)^{1/2} \tag{16}$$

$$N(E_f) = \frac{1}{2\pi^2\hbar^2}(2m_e^*)^{3/2}(E_f - E_G)^{1/2}. \tag{17}$$

As in the direct case, the absorption coefficient is proportional to the product of the final and initial densities of states, described in (16) and (17), integrated over all states separated by the energy difference $h\nu \pm E_{ph}$. It is also proportional to the probability of interacting with a phonon, a function of the number of phonons:

$$N_{ph} = \frac{1}{\exp\left(\frac{E_{ph}}{k_B T}\right) - 1}. \tag{18}$$

After integrating the products of densities of states and multiplying by the probability of phonon interaction, the absorption coefficients may be calculated as

$$\alpha_+(h\nu) = \frac{A(h\nu - E_G + E_{ph})^2}{\exp\left(\frac{E_{ph}}{k_B T}\right) - 1}, \tag{19}$$

$$\alpha_-(h\nu) = \frac{A(h\nu - E_G - E_{ph})^2}{\exp\left(\frac{E_{ph}}{k_B T}\right) - 1}, \tag{20}$$

$$\alpha(h\nu) = \alpha_+(h\nu) + \alpha_-(h\nu), \tag{21}$$

where α_+ describes absorbing a phonon and α_- describes emitting a phonon, and the sum of the two represents the net absorption coefficient.

The individual equations are not of critical importance to the present work, as a semiconductor may display several different types of band transitions, resulting in more complicated behavior than simple models would suggest. However, the general form is helpful for making sense of experimental data. In all three models discussed above. The absorption coefficient is of the form

$$\alpha(h\nu) = A(h\nu - E_G)^m. \tag{22}$$

In other words, α is always proportional to the difference between photon energy and the bandgap, to some exponent m. For direct allowed transitions, $m = {}^1/_2$, for direct

forbidden transitions $m = {}^{3}/_{2}$, and for indirect allowed transitions $m = 2$. Fitting experimental data to this model thus not only reveals the band gap but also the type of transition that is occurring.

2.2.4 Carrier Generation

Finally, the attenuation equation (6) provides a platform for calculating the generation rate of carriers at any point in the device. Assuming that each time a photon is absorbed, an electron and hole are generated, we can derive an equation for the generation of carriers G as a function of depth in the material, given an incoming photon flux of Φ. For each wavelength,

$$G = \alpha \Phi e^{-\alpha x}. \tag{23}$$

This equation will become useful later on in determining the photocurrent output of the device, which is highly dependent on the number of carriers generated.

In conclusion, photons of a wide variety of energies are incident on a solar cell. We typically approximate this range of photon energies as the AM1.5 spectrum, incorporating mostly photons in the visible spectrum. Photons with insufficient energy to create a pair of separate charge carriers are not absorbed, while photons with energy in excess of the bandgap are absorbed. Their absorption probability is affected by whether the transition is direct, forbidden, or indirect. Using this energy-dependent absorption coefficient, we can describe the frequency with which new conducting electrons are created, which is critical for determining the electrical output of our solar cell. Thus, we can fully model how incoming light leads to electricity in a Cu_2O thin film solar cell. Experimental methods in the present work will evaluate whether Cu_2O displays a direct or indirect transition at the band edge, and thus allow us to determine its absorption characteristics and bandgap. This fully explains the first stage of solar electricity generation and provides the groundwork for understanding solar cell performance.

2.3 Mobility and Diffusivity

Once electrons and holes are generated, they must diffuse towards a junction to be separated, and then to a pair of positive and negative contacts in order to be extracted. A junction effectively provides an electromotive force to separate electrons and holes, and then acts a potential barrier such that once the separated electrons and holes cross the junction, they remain apart.

Eventually, as the carriers diffuse through a solid, the negatively charged electrons will recombine with a positively charged hole. Ideally, this recombination will occur outside of the device, where the charge carriers can do useful work. If the electron and hole recombine inside the photovoltaic cell, that energy they absorbed may go to waste. Thus, understanding how quickly electrons and holes move through the semiconductor is an important precursor to understanding how well a solar cell performs.

Conduction band electrons and valence band holes can move freely throughout the semiconductor, while their oppositely charged counterparts are fixed to their host atom. These carriers tend to move through the material with an average velocity determined by their thermal energy. They move in one direction until colliding with an atom or particle in the solid's crystal lattice, and then scatter in another random direction. This describes, for the most part, the typical motion of free carriers in an unbiased semiconductor. The net displacement of each carrier is zero, as all motion is random.

However, under two different forces, drift and diffusion, carrier motion can become more coherent.

The first of these patterns, diffusion, is not so much an active force but rather a consequence of the random motion of carriers. When the concentration of carriers in one volume is greater than the concentration of carriers in a neighboring volume, on average, more carriers will move into the lower concentration half than the higher concentration half. This phenomenon of diffusion is easily understood in an analogy with gas mixing. Two neighboring compartments of distinct gases are shut off from one another. Gas molecules on each side move randomly in all directions. When the barrier is removed, gases from each side begin to randomly venture into the opposite side. As long as there is still a greater concentration of one gas in the right half, there will always statistically be more movement of that gas from right to left than vice versa. The system of two gases displays a natural tendency towards equilibrium. To get there, it displays what are described as diffusion currents.

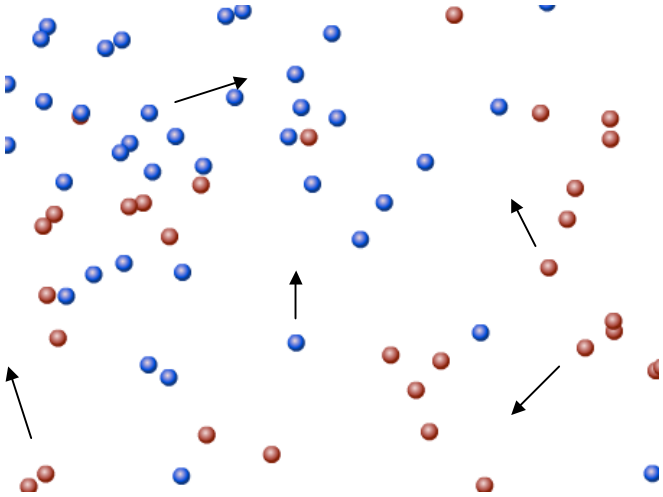

Figure 2-6: Different gas molecules, or electrons and holes, randomly mixing through randomized thermal motion [16].

Electrons and holes behave in much the same way as two distinct gases. In areas with a higher concentration of electrons than elsewhere, we will see a net flow of more electrons out than in. We can describe these differences in concentration of carriers as gradients. For one-dimensional flow, we can model the diffusion current as directly proportional to the concentration gradient of either negative or positive charge carriers [15] such that

$$J_{diff,n} = +qD_n \frac{dn(x)}{dx}, \tag{24}$$

$$J_{diff,p} = -qD_p \frac{dp(x)}{dx}. \tag{25}$$

Here, J represents the diffusion current, $n(x)$ and $p(x)$ are the volumetric densities of electrons and holes respectively, and q is the charge of a single carrier. The coefficients D_n and D_p are the diffusivity of electrons and holes respectively, with units of [cm^2/s]. This diffusivity is closely related to the conductivity of the material, which will become apparent shortly.

The second mode of carrier motion is drift current. This is the more direct effect of carriers experiencing a force under an external electric field. In addition to random thermal velocity, carriers experience acceleration in the direction of the field for positive charges, or opposite the field for negative charges. This drift current depends on the number of each carrier and the mobility of the carriers.

Mobility is a fundamentally important material property that describes how readily a carrier moves through a material under an electric field. It is measured with the SI units [$cm^2/V{\cdot}s$], indicating that it is a measure of how rapidly carriers diffuse through a cross sectional area under the influence of a potential difference. If one imagines electrons drifting at random through a lattice, they will collide with a lattice atom every time interval τ, which represents the mean time between such scattering events. After each scattering event, their average velocity is randomized, or reset to zero. Therefore the net velocity is affected by the length of time between collisions, and how much force the electric field can exert on the charge – higher charge and lower mass entities are accelerated more strongly. From this random walk theory of conductivity, we can model the mobility of charge carriers in a material as

$$\mu_x = \frac{q\tau}{m_x^*}, \tag{26}$$

where m_x^* is the effective mass of species x (either holes or electrons). The effective masses of holes and electrons can be very different, resulting in different mobilities for different charge carriers.

Mobility is a particularly useful measure in semiconductors, because it is a more specific depiction of carrier impedance than conductivity. Conductivity, a measure of charge carriers flowing through a conductor per unit time, captures both the mobility of carriers as well as the number of carriers. While not as relevant to the study of metals, these two separate phenomena are uniquely important for understanding semiconductor performance. For electrons, for example, the conductivity can be expressed as

$$\sigma = qn\mu_n. \tag{27}$$

Considering the one-dimensional conductivity of both electrons and holes in a semiconductor, we produce an expression relating drift current and electric field E,

$$J_{drift} = q(-n\mu_n + p\mu_p)E. \tag{28}$$

The competing phenomena of drift and diffusion are what drive the movement of carriers in a solar cell. At the center of each cell is a junction where, typically, two different semiconductors meet. These two materials are at different electrical potentials, and thus the junction region contains a strong electric field formed by the difference in electric potentials across the opposite sides. As carriers are formed all through the device, they tend to diffuse at random. Yet, these carriers are only useful if the negative and positive electron and hole currents can be separated, in order to form a coherent net current flow in one direction. This is where the junction plays a critical role. In the strong, unidirectional electric field at the junction, electrons and holes are forced to move in separate directions. Thus, excess electrons populate one side of the junction while the other side becomes populated similarly by excess holes. For these carriers to recombine, they now must diffuse out through another conductive path into an external circuit, doing useful work in the process.

Outside of the electric field in the junction region, carrier motion is dominated by diffusion. Thus, it is important to understand how readily carriers diffuse. In fact, the

diffusivity discussed earlier is directly related to the carrier mobility, however here the driving force does not come from an electrical potential but rather thermal energy. Relating thermal energy to kinetic energy allows us to formulate what are known as the Einstein relations [15]. These relate diffusivity and mobility as follows:

$$\begin{aligned} D_n &= \frac{k_B T}{q} \mu_n \\ D_p &= \frac{k_B T}{q} \mu_p \end{aligned} . \tag{29}$$

Mobility, and in turn diffusivity, are critically important to good solar cell performance, as we will see in the ensuing sections. Thus, measuring and understanding mobility provides a strong basis for evaluating the performance of a solar cell.

Mobility may be limited by a number of factors, which involve the phenomenon of scattering. By the definition in (26), mobility is directly proportional to the mean time interval between scattering events. Thus, the more frequently scattering events occur, the slower the carrier will move through the material and the lower its mobility will be.

The first type of scattering is phonon scattering [16]. As the temperature of the crystal lattice increases, thermal energy manifests itself in lattice vibrations where the spring-like bonds between atoms transmit acoustic waves. These waves, called acoustic phonons, can collide with electrons and holes and scatter them. The density, heat capacity, and temperature of the material affect the concentration of phonons and therefore the frequency of these scattering events.

The second variety is ionized impurity scattering [16]. A semiconductor lattice typically contains dopants, which are atoms of different valence states that introduce more electrons or holes into the semiconductor. In Cu_2O, these could typically be excess oxygen atoms that introduce additional positive charges, or other intended or inadvertent impurities such as nitrogen or iron. This introduction of donor or acceptor atoms is what changes a material's potential and therefore enables the formation of junctions, however these impurities can be problematic as well. Ionized atoms in a lattice introduce a positive or negative charge, which by Coulomb's Law can exert a force on electrons or holes. Thus the more dopants or "ionized impurities" present in the lattice, the more frequently their fields will scatter carriers and the smaller the mean scattering time will be.

While phonon and ionized impurity scattering are the dominant mobility-limiting mechanisms, there can also be smaller effects including lattice or surface defects. The cumulative effect of all of these limiting mechanisms can be summarized with Matthiessen's Rule [16],

$$\frac{1}{\mu_{total}} = \frac{1}{\mu_{phonon}} + \frac{1}{\mu_{impurities}} \ldots . \tag{30}$$

Matthiessen's Rule suggests that the mobility solely due to phonon scattering or defects can be combined to give the net mobility. In future sections, we will discuss how to measure mobility, opening the door to understanding the dominant mobility limiting mechanisms. By characterizing the mobility of Cu_2O and what limits it, we can better engineer the material to achieve more mobile carriers.

2.4 Recombination and Carrier Diffusion Length

Unfortunately, once free carriers have been created, there is a finite amount of time before they recombine. Electrons in the conduction band and holes in the valence band will recombine if given an impetus to do so. This could occur in a collision with a lattice atom, particularly at a defect site, or in a collision with a phonon or another charge carrier. Thus, it is equally important for carriers to have both a high mobility and a long lifetime to ensure that they reach a point of extraction before recombining.

Typically, three dominant sources of recombination act within a semiconductor – Shockley-Read-Hall (SRH) processes, Auger processes, or simple radiative recombination [16].

SRH recombination typically occurs in highly doped or impure materials, because it relies on the existence of many defect states. In an SRH process, an electron becomes trapped in an energy state just below the conduction band edge (or a hole just above the valence band edge) by an atom in the crystal lattice that introduces this "defect" energy level. Before the carrier has a chance to thermally escape back into its respective band, it recombines with another hole or electron that moves up or down into the same defect energy level.

An Auger recombination event involves three carriers. Here, an electron and hole recombine, but rather than release this energy as a photon or phonon, the energy is transferred into another electron in the conduction band. This electron then slowly loses this extra energy as heat as it relaxes back down to the conduction band edge. This form of recombination scales proportionally to the carrier concentration.

Finally, the simplest form of recombination is direct, radiative recombination. Here, the exact opposite of photogeneration occurs – a conduction band electron and valence band hole recombine and release a photon. This can only occur in a direct bandgap semiconductor. The photon created is typically on the order of the bandgap, so it has a high probability of escaping the semiconductor without being reabsorbed.

The more often recombination occurs, the shorter a photogenerated carrier's lifetime will be on average. As in the previous section, we can compound all of the factors limiting carrier lifetime to compute the bulk lifetime,

$$\frac{1}{\tau_{Bulk}} = \frac{1}{\tau_{SRH}} + \frac{1}{\tau_{Auger}} + \frac{1}{\tau_{Radiative}}. \tag{31}$$

Recombination is the primary mechanism to avoid in solar cell engineering, because it wastes the precious energy it took to create those carriers. It is critical to minimize the number of defects and collisions that may instigate recombination. However, carrier lifetime is difficult to measure directly and is challenging to interpret in considering solar cell performance, thus, a practical alternative is to use carrier diffusion length. Diffusion length measures how far, on average, a free carrier can be expected to diffuse through a material before recombining. It takes into account both how mobile a carrier is (i.e. how rapidly it can move through a material) and how long it lasts before recombining. The equations for electron and hole diffusion length are

$$\begin{aligned} L_n &= \sqrt{D_n \tau} \\ L_p &= \sqrt{D_p \tau} \end{aligned}. \tag{32}$$

In particular, we are interested in the minority carrier diffusion length. Cuprous oxide is inherently p-type; in other words it is dominated mostly by positively charged

holes created by excess oxygen atoms. To generate electricity, we are interested in particular in the ability of the minority carrier, electrons, to diffuse out of the material and be collected, because the electrons are orders of magnitude less common than holes in a p-type material. This elucidates the underlying design constraint for a typical solar cell. The device must be relatively thick to allow for full absorption, however it must be relatively thin such that the electrons may diffuse fully out of device before recombining. To overcome this, it is important to improve minority carrier diffusion length sufficiently to overcome the necessary thickness of the device.

The Gärtner model [17] is a common model for quantifying the effect of diffusion length on cell performance, thus it provides an effective bridge between basic material properties (mobility and lifetime) and solar cell efficiency.

We can model the maximum possible output current density as a the product of the incoming photon flux and the charge of a single carrier

$$J_{\max} = q\Phi. \tag{33}$$

We define the quantum efficiency Q_F as the ratio of actual current output to the maximum output – in other words, what percentage of photons are converted into usable electrons:

$$Q_F = \frac{J_{tot}}{q\Phi}. \tag{34}$$

Here, it is important to distinguish between external and internal quantum efficiency. The conversion of photons into electrons is not only inhibited by poor absorption or transport within the semiconductor, it is also limited by unwanted reflection and absorption before the photons can enter the active material. We therefore define internal quantum efficiency IQE as the ratio of carriers collected (output current) to the flux of photons that actually entered the semiconductor, while external quantum efficiency EQE is the ratio of output current to the total number of photons originally provided by the light source. As some of these photons are reflected off of the front of the device or absorbed by materials in transit, the EQE will be lower than the IQE. Unfortunately, it is impossible to directly measure the IQE, however by understanding the reflective and absorptive properties of the materials used, it is possible to infer the IQE from an EQE measurement.

Because we know the depth at which certain photons are absorbed (from the absorption coefficient), we know how far they must diffuse to escape the material. Thus, knowing IQE as a function of incoming photon wavelength or energy can lead directly to computing the minority carrier diffusion length.

We begin by modeling the output current density as a function of material properties. Firstly, we assume that we are dealing with a p-type material with a minority electron concentration of n_o. This p-type material is presumed to be in contact with a metal, electrolyte, or highly doped semiconductor such that the depletion region (area containing the electric field) is exclusively within the p-type Cu_2O. We assume thermal carrier generation/recombination in the depletion region is negligible, and assume that all carriers photogenerated in this region are collected. Thus, total current density is the sum of carriers generated in the depletion region and carriers that diffuse in after being generated in the semiconductor bulk:

$$J_{tot} = J_{DR} + J_{Diff}. \tag{35}$$

In the depletion region, as we assume all generated carriers are collected, we can integrate the generation rate (23) from the interface $x = 0$ to the edge of the depletion region, of width W:

$$J_{DR} = \int_0^W -qG(x)dx = -q\Phi(e^{-\alpha W} - 1). \tag{36}$$

To determine the diffusion current, we cannot assume all carriers are collected, so we must determine the current from the probability of diffusion into the depletion region. From the diffusion equation for electrons (24), we have the diffusion balance

$$D_n \ddot{n} - \frac{(n - n_o)}{\tau} + G(x) = 0. \tag{37}$$

The boundary conditions that $n(x) = n_o$ for $x = \infty$, and that $n(x) = 0$ at $x = W$, suggest a solution to (37) to be

$$n = n_o - (n_o + Ae^{-\alpha W})e^{(W-x)/L_n} + Ae^{-\alpha x}, \tag{38}$$

$$\text{where } A = \frac{\Phi}{D_n}\frac{\alpha^2 L_n^{\,2}}{\alpha(1 - \alpha^2 L_n^{\,2})}.$$

We can now solve for the diffusion current density $J_{Diff} = -qD_n n'$ at $x = W$:

$$J_{Diff} = q\Phi\frac{\alpha L_n}{(1 - \alpha L_n)}e^{-\alpha W} + qn_o\frac{D_n}{L_n}. \tag{39}$$

To demonstrate this current distribution pictorially, the depletion region and bulk region of an n-type semiconductor are depicted in Fig. 2-7, alongside the generation rate.

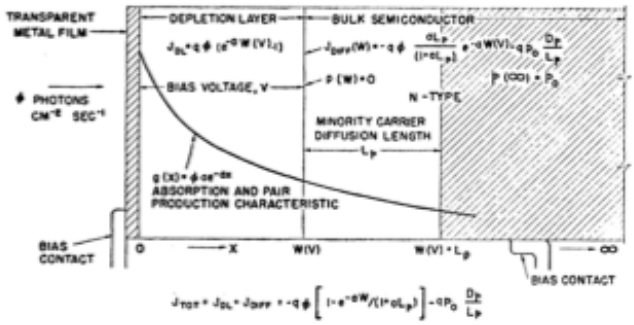

Figure 2-7: Total photocurrent is composed of current from the depletion region and diffusion current from the bulk; both currents are collected by the metal [17].

Note that the width of the depletion region can be computed from the fundamental properties of the semiconductor:

$$W = \sqrt{\frac{2\varepsilon_r\varepsilon_o}{qN_A}(V_{FB} - V)}. \tag{40}$$

To complete the model, sum the depletion region and diffusion currents such that

$$J_{tot} = q\Phi\left[\frac{1 - e^{-\alpha W}}{1 + \alpha L_n}\right] + qn_o\frac{D_n}{L_n}. \tag{41}$$

It is important to note that this current density is under monochromatic illumination (single wavelength) and the cell is under reverse bias. Forward bias performance would entail a very different current distribution. Thus, we have a functional equation expressing the expected current output from a p-type semiconductor-metal interface as a function of the electron diffusion length for each wavelength. Returning to

the definition of quantum efficiency in (34), we divide the current output by the maximum photon flux to calculate the quantum efficiency. For certain materials like Cu_2O with a sufficiently large depletion region, the boundary conditions in (37) change and the second term in (41) can be discarded for simplicity. IQE becomes

$$Q_F = \frac{1 - e^{-\alpha w}}{1 + \alpha L_n}. \tag{42}$$

This formula characterizes the effect of two material properties (carrier mobility and lifetime, summarized in minority carrier diffusion length) on the quantum efficiency of a solar cell. This is both a strong starting point for analyzing the effect of material properties on cell efficiency, as well as a useful tool for inferring material properties from measured cell output. In this case, by simply measuring the external quantum efficiency, we can calculate the internal quantum efficiency and use it to determine the minority carrier diffusion length as a result. The full utility of the models discussed above will become more apparent in the ensuing sections.

In summary, we can encapsulate the transport properties of carriers in a semiconductor with the diffusion length of carriers, as this demonstrates both the speed at which carriers diffuse and how frequently they recombine. We can manipulate the material properties to reduce sources of recombination and electrical resistance in an effort to increase this diffusion length, and in turn improve the performance of the solar cell. Given a certain absorption profile, which is largely uncontrollable by fabrication method, we can predict the magnitude of carrier generation that would occur under full illumination for different device thicknesses. Then, setting an optimal device thickness, we must engineer a material that can transport carriers across the entire thickness for extraction.

This is the path to producing a high-efficiency solar cell. The rest of the work – turning the cell into a solar panel – has been explored extensively by existing solar research. A working cell would need to be coupled with proper contacts that extract current at low resistances with minimal optical obstruction, as well as an encapsulant and glass cover that offer protective and anti-reflective properties. Thus, we begin by attacking the most fundamental problem – transport properties in Cu_2O thin films.

3. Experimental Techniques

3.1 Sample Preparation

Cuprous oxide thin films may be prepared using a number of different fabrication methods. These include oxidation of thin copper foil at high temperatures, electrolytic deposition, molecular beam epitaxy, chemical vapor deposition (CVD), and physical vapor deposition (PVD).

There are several critical challenges in fabricating a cuprous oxide thin film. Firstly, the film must be nearly stoichiometric – there must be a 2:1 ratio of copper to oxygen atoms in the material to be considered cuprous oxide. At room temperature, copper preferentially forms its bivalent oxide, CuO or cupric oxide. In light of this, it can be difficult to ensure that copper and oxygen combine in the appropriate ratio. Secondly, it is important to minimize the concentration of crystal defects in the film. This includes grain boundaries as well as point defects and impurities. With smaller crystal grains

(therefore more grain boundaries) and a higher concentration of impurities or point defects, charge carriers are more likely to encounter sites at which they can recombine or scatter. A perfect crystalline structure allows the carriers to travel largely unhindered through the material, but upon encountering a foreign species, change in crystallographic orientation, or other defect, the carriers are more likely to recombine or to change direction. In light of this, a fabrication method must aim for a thin film of high purity and crystallinity. Finally, the fabrication method must keep future production realities in mind – it must be scalable and progress at a relatively rapid rate. If thin film photovoltaics will ever scale to terawatt-level production, it cannot take prohibitive amounts of time to build up a film on the order of several hundred nanometers thick.

Unfortunately, fabrication methods that result in a high crystal quality are often the most time consuming, while quicker methods tend to result in lower quality films. Molecular beam epitaxy or high temperature oxidation tend to produce highly crystalline materials, but take much longer time periods. Meanwhile, some rapid sputtering or CVD techniques are quicker but can result in highly defective films.

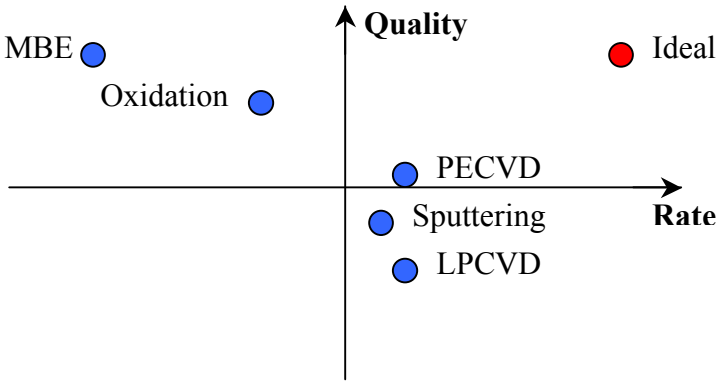

Figure 3-1: Relative quality and rate for different thin film fabrication methods including Molecular Beam Epitaxy (MBE), oxidation, Plasma Enhanced CVD, Low Pressure CVD, and Sputtering (PVD).

The present work aims to balance these competing interests by adapting a common higher-throughput method, physical vapor deposition, to produce higher quality films, and thus move towards the ideal location in the top right corner of Fig. 3-1.

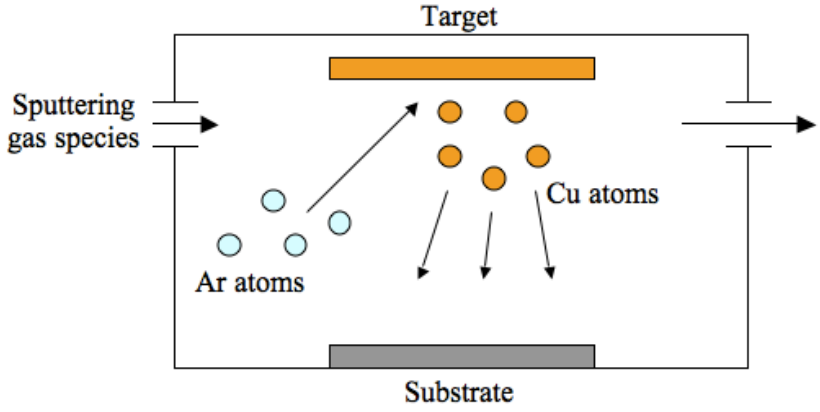

Figure 3-2: Physical vapor deposition experimental configuration.

A standard PVD setup is a closed system, evacuated or containing an inert gas species. The substrate, typically a quartz or silicon wafer, is placed at the bottom of the container. A target composed of the species to be deposited is placed on the top surface of the container, facing the substrate. Finally, the source of kinetic energy is placed facing the target. This is typically a plasma source that can fire ions or other species at high velocities towards the target. Upon impact, this beam ejects material at the surface of the target, which then strikes the substrate underneath. Fig. 3-2 displays a simplified experimental setup.

In the current work, the PVD technique used is known specifically as reactive DC magnetron (RDCM) sputtering. In reactive sputtering, the film being deposited is formed through a chemical reaction between the target material atoms and a gaseous species introduced into the chamber. This provides an efficient way of creating highly stoichiometric oxides or nitrides by using a pure metal target and an appropriate gas species. The stoichiometry of the film can be varied by the relative sputtering rate and temperature/pressure characteristics of the gas. The present work utilizes a copper target and introduces oxygen (as well as small quantities of nitrogen for doping purposes) into the chamber to produce Cu_2O thin films.

In RDCM sputtering, the source of kinetic energy comes from an inert gas plasma. For a moderately heavy atom like copper, we use argon gas. A magnetron generates a strong magnetic field that confines the plasma close to the target surface in order to speed up the sputtering process. The direct-current (DC) component refers to the fact that current is transmitted through the plasma from the target to the sample, augmenting the deposition rate and improving directionality.

For the present work, we used an ATC-2200 sputtering tool supplied by AJA International, capable of performing reactive sputtering at a wide range of temperatures and pressures on small samples on the order of 1 cm^2. The substrate used was a GE-124 fused quartz wafer, and the metallic copper target was a 99.999% pure, 2 in. diameter disc supplied by Kurt J. Lesker, Co. The atmosphere of the chamber during deposition contained argon and oxygen. Heating of the substrate was done through quartz lamps inside the chamber.

Typically, there are several disadvantages to using sputtering as a technique. Firstly, the directionality of the sputtered atoms is difficult to control, making it more difficult to maintain consistent deposition over a larger area and resulting in some variability in thickness or composition across the substrate. Secondly, the haphazard method of deposition does not lend itself to orderly crystal growth – typical low temperature sputtering methods tend to result in many small crystal grains of very different orientations. This does not present a significant problem when the film serves an optical or insulating purpose, but when we wish to deposit highly crystalline materials to achieve strong electrical transport properties, it can represent a serious challenge. Finally, sputtering is a particularly complex process as there are a broad number of parameters that may be varied.

However, this variability represents the great opportunity of sputtering – an intelligent tweaking of design parameters can result in a high degree of control over the microstructure of the film.

The particular insight that the present work attempts to leverage is that the microstructure of sputtered films is highly dependent on the deposition temperature. As

the film is deposited, separate crystal grains tend to form. With lower thermal energy available, the surface tends to form many small, fiber-like grains. At higher temperatures though, an annealing effect occurs, and the surface tends to form much larger grains. This pattern is explained thoroughly by Movchan and Demchish in the Zone Model [18], which predicts varying stages of grain formation occurring at 0.2, 0.4, and 0.7 times the melting temperature of the material. With a melting temperature of 1508 K, we selected temperatures of 300K, 600K, and 1070K. The difference is stark – Fig. 3-3 displays the difference in crystal grain size based on the substrate temperature during deposition; images are taken using an SEM. The transition from fiber-like grains to columnar grains is evident by the final panel.

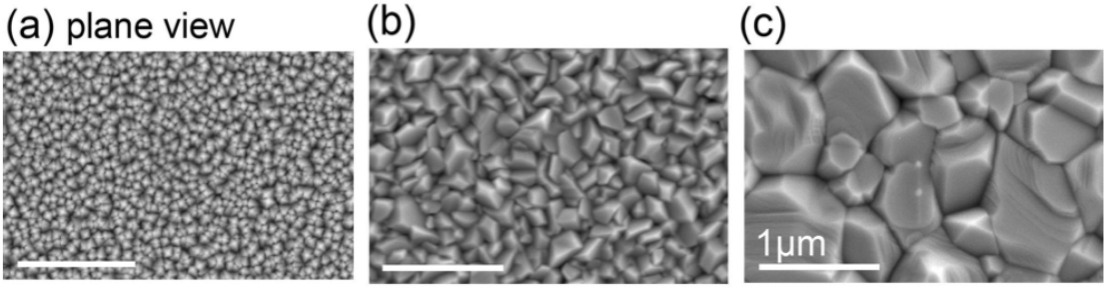

Figure 3-3: Crystal grains viewed from above for different substrate temperatures; (a) 300K, (b) 600K, (c) 1070K.

Clearly, the substrate temperature can have a profound effect on grain size. As discussed in the preceding sections, larger grain size has a direct effect on transport properties, as grain boundaries are a significant source of scattering and recombination. Thus, by utilizing these high substrate temperatures it is possible to adapt a typically lower-quality fabrication method to build high quality films while maintaining high deposition rates.

Figure 3-4: Image of the ATC-2200 sputtering tool

The particular process parameters used in film fabrication are explained in detail below. First, the substrates and target were loaded into the sputtering tool, with glass substrates physically secured by corrosion-resistant metal clips to a plate. Initially, the base pressure of the unit was set to 1.3×10^{-5} Pa, with no gas flow. Quartz lamps heated

the substrate to the desired temperature, at which point the flow of argon and oxygen began. Working pressure for deposition was 0.53 Pa and the ratio of argon to oxygen flow rates was between 1:0.35 and 1:0.39. Fine-tuning this flow ratio has measurable effects on the stoichiometry of the film. Here, the deposition rate was 3.4 nm/min, allowing the creation of a 200 nm film in less than one hour. Fig 3-4 is an image of the sputtering tool used in the present work.

After deposition, the films must be protected to avoid any mechanical damage or surface reactions. Unfortunately, at room temperatures and pressures, copper preferentially forms its bivalent oxide CuO. These films are no exception; if left exposed to the environment for extended periods of time, ambient oxygen will diffuse into the surface layer and further oxidize the Cu_2O to form a thin layer of CuO instead. This must be removed before measurements are conducted in order to ensure accuracy and repeatability.

This film is easily removed through a nitric acid (HNO_3) etch. We used 0.15 molar HNO_3 in 30mL baths to perform the etch. This solution was mixed from 2.5mL of 15M nitric acid and 250mL of de-ionized water. Typically, only the top 10nm must be removed to expose pure Cu_2O underneath, which requires a relatively short (5s) etch to achieve.

The final important step in cell fabrication is to deposit contacts for measurement purposes. We must deposit a thin layer of metal in certain regions of the device so that we have points at which to take measurements of resistivity, mobility, and current-voltage characteristics. The contacts may either by deposited on the front or back surface of the Cu_2O.

The present work employs gold contacts as gold does not react with Cu_2O and does not cause adverse charge build-up at the interface with the semiconductor. Front contacts are useful for mobility measurements, and were deposited in small squares at the four corners using e-beam evaporation and an aluminum mask. A back contact is more useful for optical measurements, as it prevents optical obstruction of the front surface. For this configuration, a 300 nm gold layer was sputtered onto the quartz wafer before the Cu_2O deposition occurred, to provide a complete back contact.

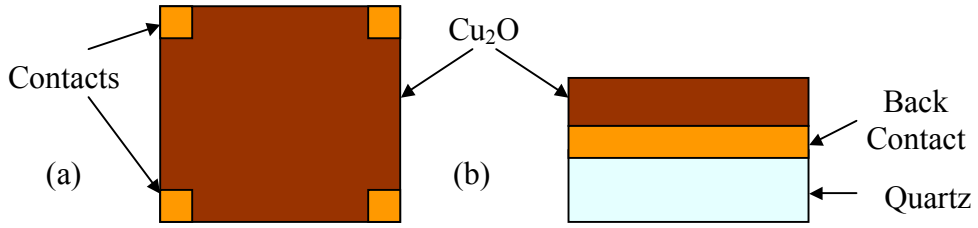

Figure 3-5: Gold contact locations for (a) front and (b) back contacts.

In summary, we deposit our Cu_2O thin films through a high-temperature reactive sputtering process, in which copper atoms are ejected at high velocities and react at elevated temperatures and pressures with oxygen atoms in transit, forming a thin film of relatively high purity and crystallinity on the wafer surface. Ideally, this fabrication method can result in high quality films that could not only achieve higher solar conversion efficiencies but are also easily fabricated at the scale of 1 m^2 solar panels.

3.2 Spectrophotometry

To determine the absorption coefficient as well as a number of other material properties including film thickness, we use a technique known as spectrophotometry.

A spectrophotometer is used to measure the transmissive or reflective properties of a material as a function of wavelength. Typically, a spectrophotometer employs a broadband radiation source, which for solar measurements must supply ultraviolet, visible, and infrared light. A monochromator is used to selectively emit a narrow band of this spectrum (on the order of the wavelength of light), and can be tuned to scan the entire spectrum.

For detection, the spectrophotometer uses photometer, which can measure the intensity of a light source with high precision. Reflected or transmitted light is first collected in a reflecting sphere, where it eventually strikes the photodetector. This measurement can separately detect either reflection off of a surface or transmission through an object, depending on the configuration.

The tool used in the present work is a Perkin Elmer Lambda 950 UV/VIS Spectrometer, pictured in Fig. 3-6. This spectrophotometer uses a single beam source, which means that to take a measurement, a baseline calibration must be referenced each time, in order to obtain accurate readings.

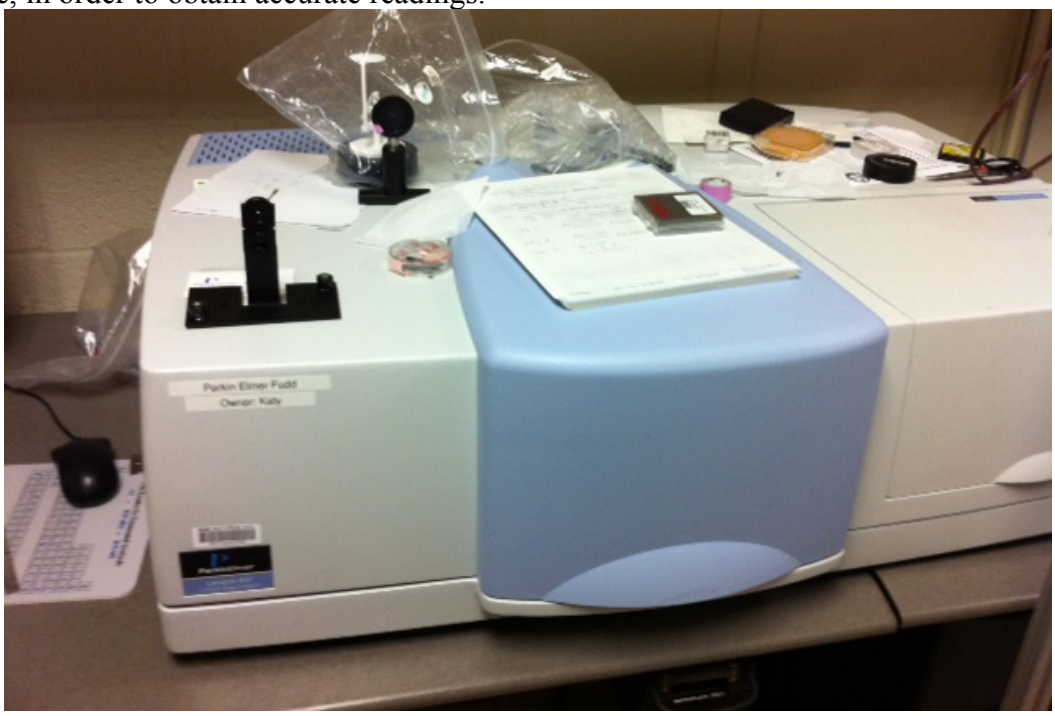

Figure 3-6: Perkin Elmer Lambda 950 Spectrophotometer used in the present work.

Inside, the spectrophotometer includes a light source, monochromator, lenses for concentrating the beam, and a Spectralon reflecting sphere with two apertures and a photometer. Fig. 3-7 displays the basic configuration used for both reflection and transmission measurements.

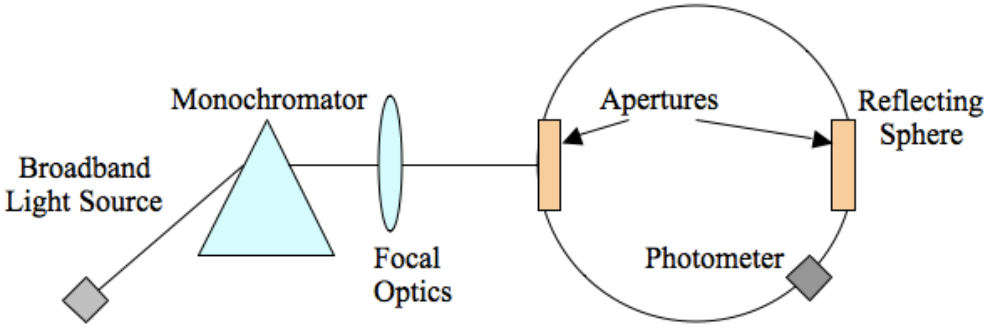

Figure 3-7: Diagrammatic view of the inside of a spectrophotometer, displaying the source of illumination and method for recording information.

The reflection measurement compares the relative light intensity reflected (in units of power) to the incident light intensity at each wavelength of light. This gives a non-dimensional fraction or percent, ranging from 0% for a perfectly black body to 100% for a perfect reflector. The Spectralon material used in the reflecting sphere is a fluoropolymer with the highest diffuse reflectivity of any coating, with reflectance $R >$ 99% across the visible and near-visible spectrum. It is therefore an ideal material with which to coat the reflecting sphere, as it minimizes losses that may occur when collecting scattered light. It is also highly useful as a baseline calibration material.

In a reflection measurement setup, the sample of interest is placed on the far side of the reflecting sphere from the incident light source. Light enters the sphere as a coherent beam, striking the sample and scattering at all angles. It is important for the light source to be slightly offset from directly normal to the sample, as otherwise the reflected light could readily escape back out the entrance aperture. The reflected photons scatter throughout the sphere, potentially undergoing many collisions due to the diffuse nature of Spectralon before striking the photometer. Fig. 3-8 illustrates the photon collection process.

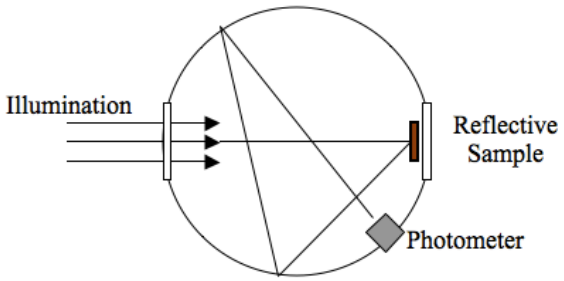

Figure 3-8: Spectrophotometer reflectance measurement setup.

To obtain an accurate intensity measurement, it is important to reference a baseline reflection. To do this, we compared the reflection off of the sample to a near-perfect reflector (also made from Spectralon). By scanning both the Spectralon reflector and thin film sample with the same illumination and same wavelengths, one may establish what fraction of the full intensity was reflected by the sample. This measurement resulted in a two-dimensional reflectance plot with wavelength on the abscissa and reflected intensity (non-dimensional, 0-100%) on the ordinate.

Transmission measurements require a subtly different setup. Here, the sample is placed at the entrance to the reflecting sphere, and the rest of the sphere is completely sealed off with high reflectivity Spectralon. Light incident on the sample may be reflected, absorbed, or transmitted through. Any light transmitted through the sample ends up in the reflecting sphere, and as before, finds its way to the photometer. The configuration for this measurement is pictured in Fig. 3-9.

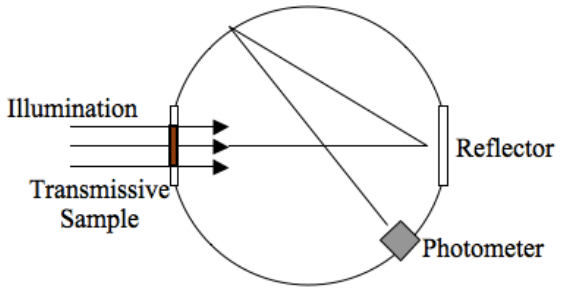

Figure 3-9: Spectrophotometer transmittance measurement setup.

Here, the photometer was initially calibrated for 100% transmission. An initial measurement was taken with no sample placed at the entrance aperture. Then, the sample transmission measurement was referenced to this 100% case to determine the fractional intensity transmitted by the sample. As in the reflection measurement, the final result is a plot, comparing wavelength on the abscissa with transmittance (fraction of light intensity transmitted, 0-100%) on the ordinate.

These two plots contain the data to determine two critical pieces of information. Firstly, the thickness of the film may be determined through Fabry-Perot methods.

A simple Fabry-Perot interferometer involves a thin film of a different index of refraction placed between two other transmissive materials. Light incident on the first surface may either be reflected or transmitted. Neglecting absorption, this transmitted light may then be reflected off of the back of the film, or transmitted through. This process of reflection within the thin film could continue ad infinitum, but we are interested primarily in the first two reflections, illustrated in Fig. 3-10.

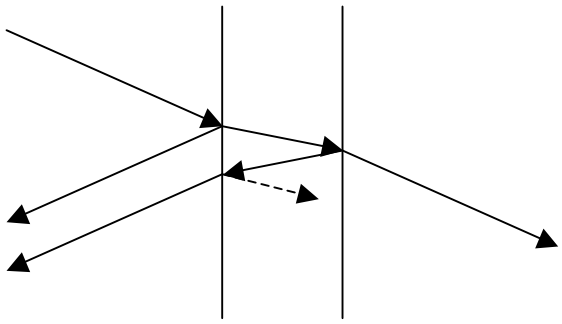

Figure 3-10: Fabry-Perot interferometer displaying dual reflected waves off of the front and back surfaces of a thin film.

These two reflections off the front and back surface of the film are both recorded by the photodetector, and interfere to form a superposition of the two waves. However,

one wave has traveled an extra distance equal to twice the film thickness, and thus emerges with a phase delay relative to the first reflection.

Two superimposed sinusoidal waves can result in either constructive, or destructive interference. If the two sinusoids are in phase, their maxima line up and the cumulative wave appears more intense due to the combined field strength. However, if the sinusoids are half a period out of phase, the minima of one wave will align with the maxima of the other. When this happens, the two waves destructively interfere, resulting in an attenuated intensity due to the subtraction of one wave's field from the other. For any phase differences in between these two extremes, partial interference occurs. Thus, if the optical path length in the thin film is equal to a multiple of the light's wavelength λ, we expect to see a constructive interference. Likewise, if the optical path length is equal to $\lambda/2$ more or less than a multiple of λ, we expect to see destructive interference. Indeed, the observed reflectance plot displays a characteristic periodic pattern as a function of wavelength.

$$2n_{film}d = \left(m - \frac{1}{2}\right)\lambda, \text{ for constructive interference,} \tag{43}$$

$$2n_{film}d = m\lambda, \text{ for destructive interference,} \tag{44}$$

$$m \in \mathrm{Z}.$$

To determine the thickness of the film, a computer algorithm solves the two equations simultaneously with a neighboring peak and trough, first solving for m and then back-tracking to find d. This could also be done by hand.

Secondly, we can determine the absorption coefficient as a function of wavelength from the reflectance and transmittance information. In aggregate, the energy absorbed is equal to

$$A\% = 100\% - R\% - T\%, \tag{45}$$

where R and T are the measured reflectance and transmittance, however it is more useful to calculate the percentage of non-reflected energy that is absorbed over the length of the sample. This provides a formula for the absorption coefficient α specifically, as a function of the film thickness d and the reflectance and transmittance at each wavelength:

$$\alpha = \frac{-\ln(T/(1-R))}{d}. \tag{46}$$

Now, we have the absorption coefficient as a function of photon wavelength or energy, which may be compared to the band-edge models discussed in section 2.2. By fitting equation (22) to the data simultaneously for bandgap and exponent m, it is possible to determine the form of band-edge transition occurring (direct, forbidden, or indirect) and calculate the magnitude of the bandgap.

3.3 Hall Effect Mobility

As discussed in Section 2.3, the charge carrier mobility, μ, is a critical property for understanding solar cell performance. It enables separation of the readily observable and simple concept of conductivity into its constituent factors – number of free charge carriers available, and how easily free charge carriers move through the material. Unfortunately, it is extraordinarily difficult to measure the mobility of minority carriers (electrons in Cu_2O), as they make up a small fraction of charge carriers in an unbiased material. Recalling the equation for conductivity,

$$J_{drift} = q(-n\mu_n + p\mu_p)E\,, \tag{47}$$

if p>>n therefore our conductivity measurements will almost exclusively be measuring majority carrier movement. Nonetheless, measuring majority carrier mobility can still give us insights into the Cu_2O film's microstructure and how readily majority and minority carriers may be transported throughout the material.

The Hall Effect technique is perhaps the most reliable and proven way of measuring majority carrier mobility, and is used in the present work to characterize cuprous oxide.

The Hall Effect represents the manifestation of the Lorentz force in a solid. As an extension of Faraday's law of induction, Hendrik Lorentz established in 1892 the existence of what we now know as the Lorentz force:

$$\vec{F} = q\left[\vec{E} + (\vec{v} \times \vec{B})\right] \tag{48}$$

Moving charges not only experience forces due to electric fields, but also due to magnetic fields as long as the charge is in motion. The direction of this Lorentz force is perpendicular to both the trajectory of the charge and the magnetic field, expressed as the cross product of these two vectors. This phenomenon causes charges to rapidly change direction as they are forced perpendicular to their path, as seen in Fig. 3-11. This phenomenon is commonly used to control charged particles in accelerators and detectors.

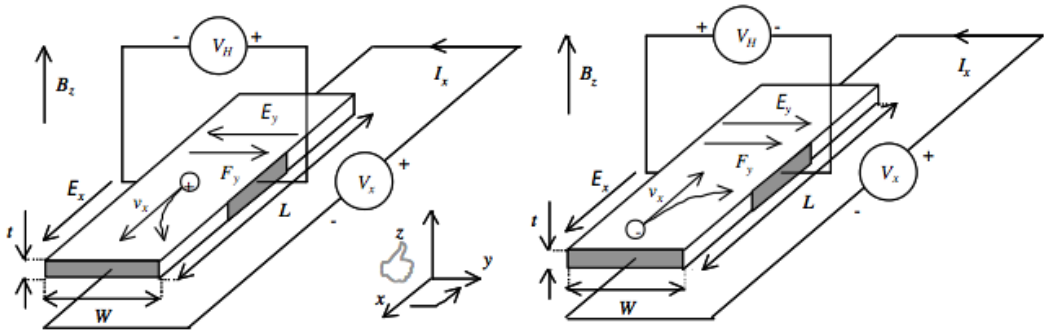

Figure 3-11: Hall Effect displacing charges by an external magnetic field imposed (left) in n-type semiconductors, (right) in p-type semiconductors [19].

Within a solid semiconductor, there could be on the order of 10^{15}-10^{19} free carriers of the same charge moving under an electric field, and thus the Lorentz effect should be readily visible at a macroscopic level. Indeed it is, and it is this phenomenon that is referred to as the Hall Effect.

As charge carriers move through a conductor under the influence of an electric field, a magnetic field may be placed across the current flow, forcing carriers to change direction. If we pass current through a material under a magnetic field, we expect to detect a subtle Hall Effect voltage V_H in the perpendicular direction. To infer mobility from this measurement, there are two distinct steps [20].

First, we must determine the resistivity of the film through a Van der Pauw sheet resistance measurement. We use a square sample with four ohmic contacts deposited at the corners as in Fig. 3-12. The contacts will be referred to as A, B, C, and D as labeled.

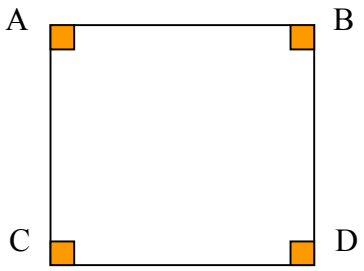

Figure 3-12: Ohmic contacts at the four corners of the film sample.

Using four microprobes, contact is made to the four corners through a computer that may send signals through the probes or read data from them. This is known as a 4-point probe measurement setup and will be used for both the Van der Pauw and Hall Effect measurements. For the Van der Pauw resistivity measurement, a set current I is passed through the sample from contact A to B, while the resulting voltage drop V is measured between contacts C and D to give the ratio

$$R_{AB,CD} = \frac{V_{CD}}{I_{AB}}. \quad (49)$$

Performing this measurement in two different directions gives two different Van der Pauw coefficients, which may be used to find the sheet resistance R_S. The average of the two x-direction measurements forms R_A, while the average of the two y-direction measurements forms R_B.

$$e^{\left(\frac{-\pi R_A}{R_S}\right)} + e^{\left(\frac{-\pi R_B}{R_S}\right)} = 1 \quad (50)$$

is solved iteratively for R_S. Given the sheet resistance, which has units of Ohms [Ω], it is possible to calculate the resistivity of the film by multiplying by the height of the film through which carriers travel, t, to give

$$\rho = R_S t. \quad (51)$$

The next step is to perform the Hall Effect measurement. In this 4-point probe setup, the current is injected diagonally from electrode A to D, while the voltage is measured in the perpendicular direction between contacts B and C. During the measurement, a strong magnetic field of magnitude B is applied normal to the film.

The Hall coefficient is then defined based on the measured voltage and the width between contacts, w:

$$R_{H,A} = \frac{wV_{BC}}{BI_{AD}}. \quad (52)$$

This Hall coefficient is calculated four times with the same current and magnetic field strength, for each possible diagonal configuration. The average of these four values, R_H, is then calculated. Now, we have both the Hall coefficient and resistivity, which combined give us the Hall mobility of majority carriers (holes for Cu_2O) in the material

$$\mu_{\text{Hall}} = \frac{R_{\text{H}}}{\rho}. \quad (53)$$

In addition, the concentration of charge carriers may be computed as

$$p = \frac{1}{qR_H}. \quad (54)$$

To execute this particular experimental procedure, it is necessary to be able to suspend a thin film sample perpendicular to a magnetic field while maintaining electrical contact to conduct measurements. This is accomplished in the present work through a pole electromagnet and custom-fabricated sample holder to position the thin film, both of which are pictured in Fig. 3-13.

Figure 3-13: Magnetic sample holder setup displaying (right) the sample holder complete with 4-point probe chip connected to triaxial plugs, gaussmeter port, and enclosure for stability and light blockage, and (left) the sample holder suspended between two electromagnet poles.

The magnet used is a 4" diameter AML pole electromagnet, and it can achieve up to 15000 Gauss or 1.5 Tesla in field strength at 30A of current. The chip and sample holder were fabricated in house, and the measurements were conducted with a Keithley Interactive Unit and a gaussmeter probe.

There are several complicating factors to consider when conducting this measurement. Firstly, there is significant noise present due to ambient radiation or variations in the applied fields that may result in a time-varying signal. Because of the very weak output voltages measured, it is important average over several measurements to limit the effect that the weak signal-to-noise ratio may have on the observation. Additionally, measurements may not be performed for an extended period of time or with large current values, as joule heating will disrupt the highly temperature-dependent results.

A second complicating factor is that the permanent magnet used displays a significant magnetic remanence of approximately 3900 Gauss, such that when the electromagnet turns off, there is still a field in the air gap. Thus, it is not possible to take zero-magnetic-field measurements in the setup, which may complicate calibration efforts. Resistivity measurements, as a result, are typically done outside of the magnet.

Finally, the path between the microprobes and the semiconductor, through the thin gold contact, provides a small amount of resistance. This contact resistance, if assumed to be due to the semiconductor, will skew the resistivity values calculated. Thus, it is important calibrate beforehand with a series of contacts spaced at specific distances apart, measuring the resistance between them. For an ohmic contact, the slope of the resistance vs. distance traveled through the material is constant. Fig. 3-14 displays this resistance plot.

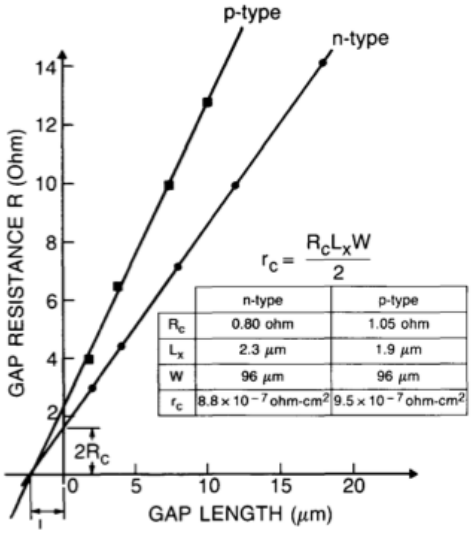

Figure 3-14: Ohmic contact resistance is found where the graph intersects the ordinate in this plot of resistance vs. contact separation [21].

Projecting the plot back onto the ordinate, we can infer what the resistance would be were the contact gap zero, which gives the exact resistance of the two contacts. This resistance must be discounted during the actual Van der Pauw and Hall Effect observations in order to focus on the properties of the Cu_2O film.

In summary, we employ a 4-point-probe measurement setup to test the resistivity and mobility of majority carriers in our thin films. With proper calibration steps and averaging, it is possible to achieve highly repeatable and accurate measurements of the transport properties of our Cu_2O films.

3.4 Photoelectrochemical Cell for Diffusion Length

To measure the current output of our thin films in order to evaluate the quantum efficiency, current-voltage characteristics, and diffusion lengths in our sample, we must form a junction with the Cu_2O. As we cannot fabricate n-type Cu_2O, we must make this junction through alternative methods. One common alternative to a p-n junction is a Schottky junction, or an interface between a metal and semiconductor. The behavior of such an interface was described in detail in Section 2.4 and is useful for such material characterization for its ease of fabrication and relatively simple modeling.

However, most conductors are opaque and thus interfere with the transmission of photons into the semiconductor. Additionally, it is difficult to find metals that do not react with Cu_2O at the surface.

One alternative to a metal-semiconductor junction is to use an electrolyte-semiconductor interface. Here, we use a liquid that contains free ions, which enables it to be highly conductive. This enables complete electrical contact with the semiconductor surface to collect the photogenerated carriers, without depositing any additional material on the Cu_2O thin film. Additionally, electrolytes tend to allow optical access because of their transparency, ensuring that most incident photons make it to the Cu_2O surface. Because of the high conductivity of the electrolyte, it can be modeled exactly like a metal-semiconductor interface, allowing us to use the same equations as derived through the Gärtner model in Section 2.4.

To measure the transport properties of our thin films we employ a photoelectrochemical (PEC) cell. A PEC cell consists of a hollow cavity containing a specific electrolyte, a transparent aperture for illuminating the sample, and an opening on the opposite side at which the semiconductor is placed in contact with the electrolyte. A magnetic stir stick is placed within the liquid and is used to speed up the transmission of charge carriers through the electrolyte. A platinum electrode is also placed in the cavity to extract the carriers from the liquid. An additional contact is made with the semiconductor to complete the circuit and allow us to bias the electrolyte-semiconductor junction. This set-up is demonstrated schematically in Fig. 3-15.

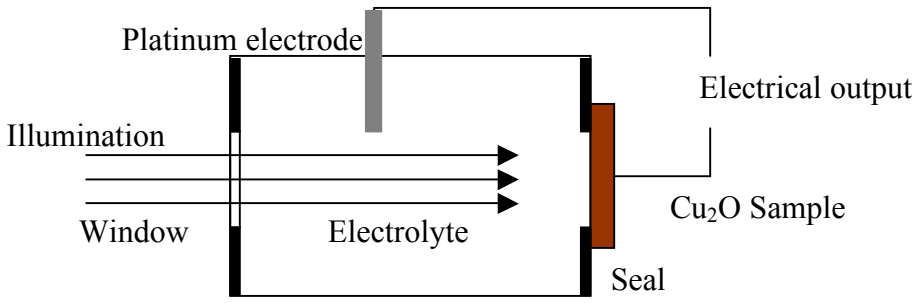

Figure 3-15: Schematic setup for a photoelectrochemical cell.

The PEC cell used for this experiment is a PN4300PC Electrochemical C-V profiler purchased from Accent, and is displayed here in Fig. 3-16.

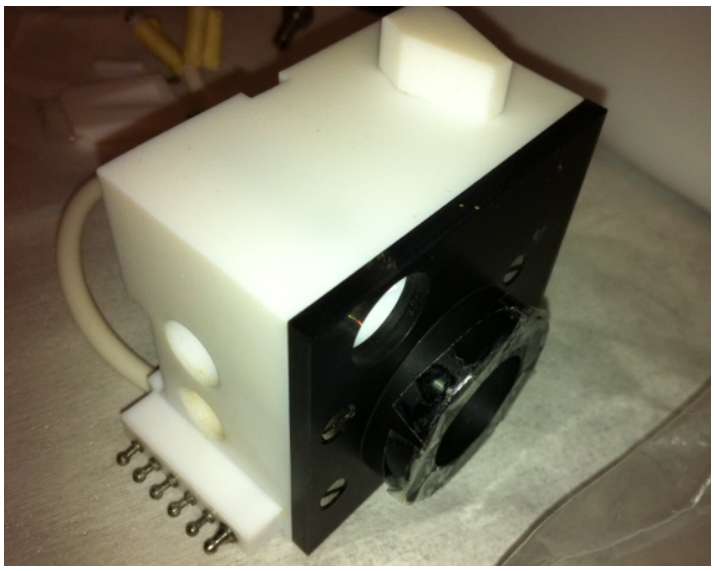

Figure 3-16: PEC used in the present work, as viewed from the front aperture.

To achieve results from this PEC setup, it is very important to select an appropriate electrolyte. In general, the electrolyte must not cause significant optical losses, and must provide a sufficient concentration of ions to enable electrical conductivity. Furthermore, the reduction-oxidation (redox) potential of the electrolyte must be compatible with the semiconductor it is paired with. The redox potential is a corollary of the Fermi level for semiconductors or work function for metals – it provides a sense of the relative energy required to add or remove charges. An ideal PEC cell setup

would match the redox potential of the electrolyte to the Fermi level of the semiconductor. If these two values are significantly different, it will distort the energy bands at the junction and force the junction to operate in a breakdown or highly resistive regime. A closely matched redox potential instead results in moderate band bending to promote current flow.

Cu_2O happens to have a particularly large electron affinity, with a conduction band edge 3.2 eV below the vacuum level [22]. It therefore requires the use of an electrolyte with a particularly large redox potential. It is difficult to find an appropriate electrolyte with this redox potential that is also chemically compatible with Cu_2O, and that does not result in any surface deposition or etching when in contact. Prior literature suggests that a working electrolyte is the decamethylcobaltocene$^{+/0}$ redox couple [22], for its particularly large redox potential and chemical stability in contact with Cu_2O.

This particular redox couple requires the use of four chemicals: acetonitrile (CH_3CN) as a solvent, 1.0 M lithium perchlorate ($LiClO_4$), 0.0020 M bis(pentamethylcyclopentadienyl) cobalt(III) hexafluorophosphate ($Me_{10}CoCp_2^+$), and 0.0002 M bis(pentamethylcyclopentadienyl) cobalt(II) ($Me_{10}CoCp_2^0$). Chemicals for the present work were purchased from Sigma Aldrich, and typically require a high degree of purity for a successful electrolyte production.

CH_3CN (anhydrous, 99.8% purity) must be distilled under high-purity nitrogen gas from CaH_2. Battery grade $LiClO_4$ (99.99% purity) was used, and must be dried by fusion at 350ºC and <1 milliTorr, followed by storage in a <0.2ppm O2 environment. $Me_{10}CoCp_2^+$ comes in powder form and must be recrystallized before use. Finally, $Me_{10}CoCp_2^0$ in powdered form must be purified by sublimation. For the purposes of the present work, these advanced purification steps were not undertaken due to material and equipment limitations. The electrolyte was formed from the chemicals as purchased.

The electrolyte was mixed in a glove box filled with nitrogen gas at above-ambient pressure. Exposure to oxygen degrades the chemicals used, so the glove box was maintained at below 100ppm of oxygen during mixing and below 5ppm during storage. Chemical quantities were measured by mass then mixed into 30mL of CH_3CN using a magnetic stirring apparatus. It was necessary to mix the $Me_{10}CoCp_2^+$ first and to stir for at least 10 minutes to ensure complete dissolution of each species, in particular the large quantity of $LiClO_4$. Exact masses are tabulated below for different volumes.

Table 3.1: Quantity of chemicals necessary for different mixture volumes.

Chemical	Molar Mass (g/mol)	Quantities		
CH_3CN	N/A	10.0 mL	20.0 mL	30.0 mL
$LiClO_4$	106.39	1.064 g	2.128 g	3.192 g
$Me_{10}CoCp_2^+$	329.39	0.007 g	0.013 g	0.020 g
$Me_{10}CoCp_2^0$	474.35	0.001 g	0.002 g	0.003 g

Now, minimizing potential air exposure, the electrolyte was loaded into the PEC cell. A Cu_2O film was placed at an aperture sealed by o-ring to provide the semiconductor-electrolyte junction. Finally the circuit was completed by a platinum electrode placed in the liquid and a gold contact at the back side of the Cu_2O film. A magnetic stirring stick was rotated at >1000rpm to promote movement of charge carriers in solution. In doing so, the mass transport time of ions in the fluid is reduced.

Several measurements are possible now with an assembled PEC cell. In the present work, we conduct three specific measurements.

First, we graph the photoelectrochemical cell's current-voltage curve. For a semiconductor-electrolyte junction, the current-voltage characteristic is subtly different from a standard diode. At equilibrium the redox potential of the electrolyte will try to align with the Fermi level of the semiconductor, producing subtle band bending if the materials are well matched. For a p-type semiconductor, a depletion region of negative charge will form at the semiconductor surface, producing the band configuration seen in Fig. 3-17.

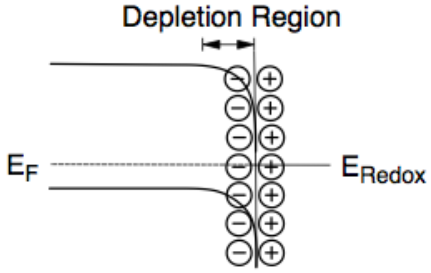

Figure 3-17: Band bending and depletion region at zero bias for a p-type semiconductor, with the electrolyte on the right [12].

When applying negative potential to the semiconductor (negative bias), this band bending is accentuated, resulting in a larger depletion region. In positive bias, the bend bending is reversed, resulting in an accumulation region of excess holes forming at the junction. At a specific potential in between, however, the Fermi energy lies at the exact same energy as the electrolyte's redox potential. When this occurs, the band edges flatten out and no accumulation or depletion occurs. This is known as flat-band potential V_{FB}. Fig. 3-18 demonstrates the band progression at different biases.

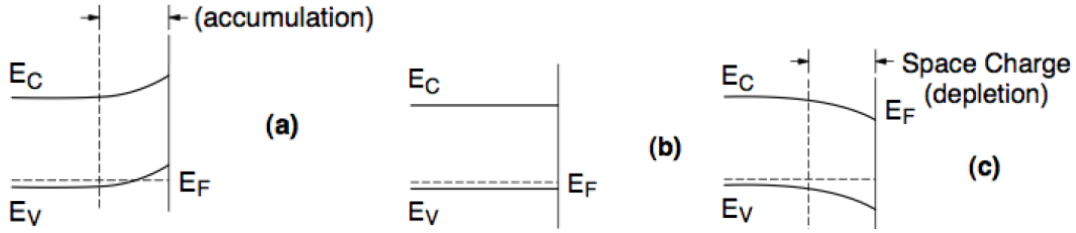

Figure 3-18: Band bending at different biases for a p-type semiconductor (a) forward bias, (b) flat-band, (c) reverse bias [12].

The existence of this flat band potential creates a unique I-V curve for such junctions. In the dark, the curve resembles a diode. Under illumination, where a diode would experience a photocurrent shift of the entire curve, only the voltages below the flat band potential experience a photocurrent shift. This phenomenon is illustrated in Fig. 3-19.

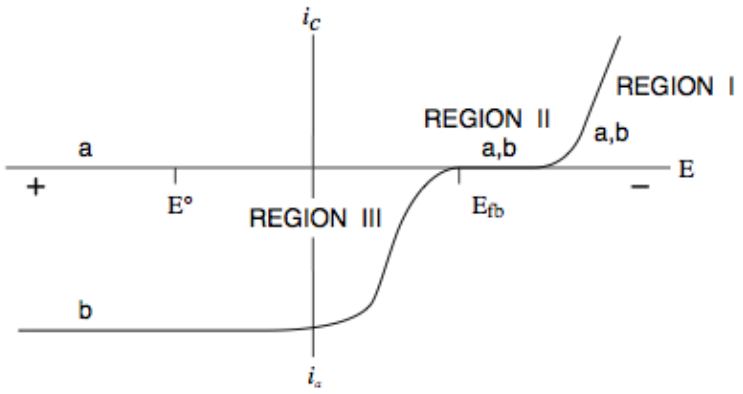

Figure 3-19: I-V curve for an n-type semiconductor-electrolyte junction demonstrating flat-band potential and the effect on illumination, (a) unilluminated curve, (b) illuminated curve [12].

To demonstrate this phenomenon and to view the photoresponse, we measured the output current of the PEC cell at 0.1 V intervals from -0.8 V to +0.8 V. Measurements were taken after 5-10 seconds when the current had achieved a steady state value, as there is some mass-transport delay of charges through the liquid. The measurement was performed both unilluminated and illuminated with a 100 W broadband incandescent light source.

Secondly, to determine the exact magnitude of the flat-band potential, we performed a second test to define a Mott-Schottky plot. A Mott-Schottky plot graphs the applied potential on the abscissa and the inverse of the capacitance squared on the ordinate. The plot should be linear with a negative or positive slope for a p-type or n-type semiconductor respectively. The flat-band potential may be found by extrapolating to the intersection with the voltage axis, or where $1/C^2 = 0$. This voltage is related to the flat-band potential and available thermal energy [23]:

$$V(1/C^2 = 0) = V_{FB} + \frac{k_B T}{q} \tag{55}$$

Finally, we performed a diffusion length measurement on the sample. We select a wavelength range to sample, encompassing the full spectrum. In particular, photons with energy greater than 1.9 eV are of use. The absorption coefficient for each wavelength has already been measured and will be of use in performing the calculation. We began by calibrating the measurement with a photodiode, for which the correlation between number of incident photons and output current is already established.

Subtracting the optical losses from absorption in the electrolyte and reflection off of the sample (calculated for this specific wavelength), we then used the calibration data to determine the number of photons expected to be incident on the Cu_2O surface. This allows us to calculate the internal quantum efficiency.

We then applied a range of bias voltages and measured the output current. Later, we selected the bias voltage that placed the device in saturation, thereby putting out the maximum photocurrent.

Now, we may insert our quantum efficiency data into equation (42). Given our known absorption coefficients, there are only two remaining variables – depletion width W and the diffusion length L_n. W may be computed from the fundamental properties of Cu_2O and the dopant density, leaving L_n as the sole variable. By iterating through

different values of L_n, we can fit the quantum efficiency curve to our measured values and find the exact quantity for minority carrier diffusion length L_n at different bias voltages. We then determine the location of the saturation region to ensure that we are taking the diffusion length calculated at the maximum current output.

In summary, we constructed an electrolyte-semiconductor junction in order to perform current-voltage tests on the Cu_2O film. By employing an electrolyte with a high redox potential and optical transparency, we can form an operating junction with Cu_2O. Finally, we gathered I-V characteristics, Mott-Schottky plots, and diffusion length measurements from the cell through several different experiments.

4. Results and Analysis

4.1 Test Sample

To examine the accuracy of our testing method, we began by testing a Gallium Arsenide (GaAs) sample with well-documented properties.

The sample was diamond-scribed and cut from a 300 nm GaAs wafer down to a 1cmx2cm rectangle for use in the PEC cell apparatus. Additionally, a thin 10nm back contact of gold was deposited to form an electrical contact with the GaAs.

Two separate PEC cell tests were run using two different electrolytes. First, a diffusion length calculation was performed using HCl as the electrolyte. Secondly, an I-V measurement was performed with the decamethylcobaltocene$^{+/0}$ redox couple electrolyte, which is also compatible with GaAs.

Placing the GaAs-HCl junction under illumination, the cell was biased with voltages from 0.0 V to -0.5 V (0.1 V intervals) over the wavelength range 300nm-850nm (intervals of 50nm). Current output, averaged over 20 seconds, was recorded for each wavelength, then repeated for each voltage interval. This current vs. wavelength data at different biases was then substituted into a MATLAB program designed to follow the equations listed in Section 2.4. Fig. 4-1 demonstrates the output of this scan in two plots – the current output as a function of time during the wavelength scan, and the resulting quantum efficiency calculated.

Given this data, a MATLAB program solves for diffusion length at each bias. In particular, we would like to use the diffusion length measurement from the saturation current region. Performing a Mott-Schottky plot for GaAs, we determined the flat-band potential to be approximately -460 mV. Thus, at voltages in the -100 mV to +100 mV range, the GaAs is expected to be in saturation. Solving for the diffusion length at 0 V, over the entire wavelength spectrum, yields a minority carrier diffusion length of 0.41 microns, or 410 nanometers. This closely correlated with values previously obtained with similar samples, suggesting that the experimental setup and MATLAB program were both repeatable and accurate. Thus, the measurement should provide reliable data for the new, Cu_2O samples.

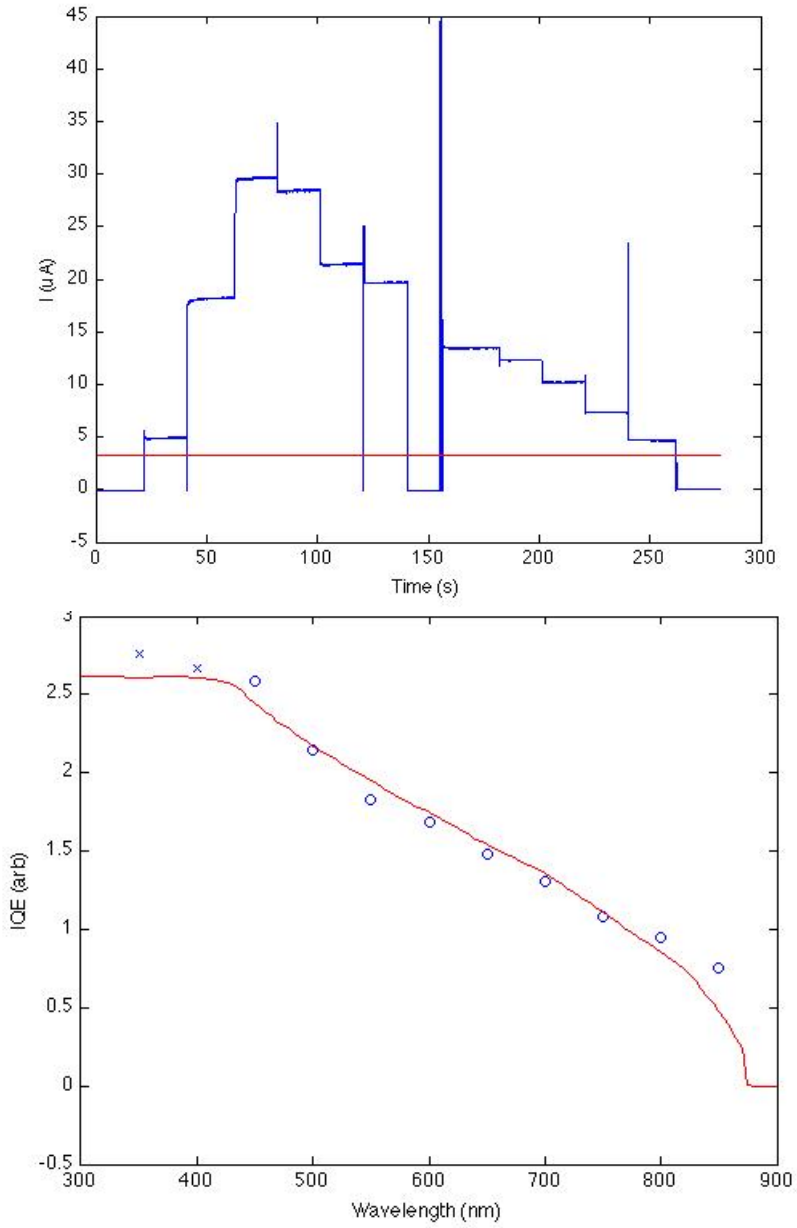

Figure 4-1: Wavelength scans performed at -200 mV bias. (top) Plots the current output in micro-Amps as the wavelengths are scanned; (bottom) plots the internal quantum efficiency as a function of wavelength based on the current output.

The second test performed involved determining the I-V characteristic in unilluminated and illuminated (100 W broadband source) conditions using the same GaAs sample and the decamethylcobaltocene$^{+/0}$ redox couple. Sweeping through voltages from -0.8 V to +0.8 V with an interval of 0.1 V, the current was measured at each step. This current measurement was taken 5-10 s after the start of each interval to insure a steady-state value given the mass transport effects in the electrolyte. Fig. 4-2 displays the resulting dark and illuminated I-V curves.

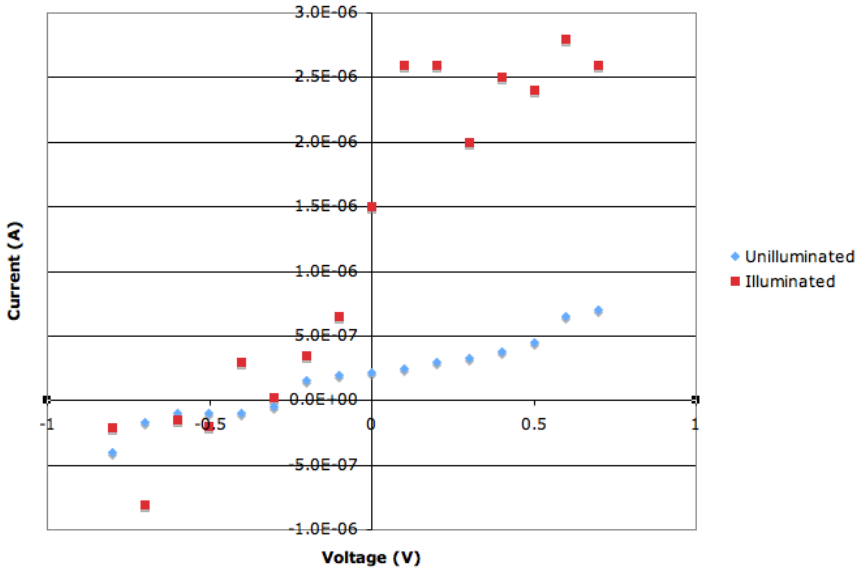

Figure 4-2: I-V curve, dark and illuminated for GaAs and cobaltocene pair.

Despite the noise in the plots, the junction is clearly demonstrating Schottky diode performance with a photocurrent appearing only above the flat-band voltage. Here, the flat band voltage appears to be around -0.5 V, closely matching the value calculated in the previous experiment. In addition, a photocurrent of significant intensity is clear, indicating that the electrolyte is certainly capable of collecting charge at the semiconductor interface and transferring it to the platinum electrode.

In summary, the results of the initial GaAs test runs showed positive results, with flat-band potential and minority carrier diffusion length calculated with accuracy. In addition, a strong photoresponse provided a clear view of Schottky diode I-V performance as Cu_2O is expected to perform as well.

4.2 Absorption Measurement

The first measurement performed on Cu_2O films involves spectrophotometry to determine film thickness and to determine the band-edge transition properties.

Reflection and transmission measurements were taken on the Cu_2O thin film and are plotted as measured in Fig. 4-3.

The reflectance and transmittance characteristics display clear Fabry-Perot interference for smaller photon energies insufficiently energetic to be absorbed. Multiple reflections off of the front and back of the Cu_2O film yield a periodically varying interference pattern. As the photon energy surpasses the bandgap around 2 eV and absorption begins, the transmittance begins to drop substantially; as this occurs, it limits the magnitude of the second reflection off of the back of the Cu_2O film, which prevents Fabry-Perot interference from occurring.

The first piece of information that may be interpreted from these plots is the film thickness. By supplying the spectrophotometer program with the reflectance, transmittance, and index of refraction as a function of wavelength, the program fits the data to determine the film thickness. For this sample, we determine that the film thickness is 268 nm.

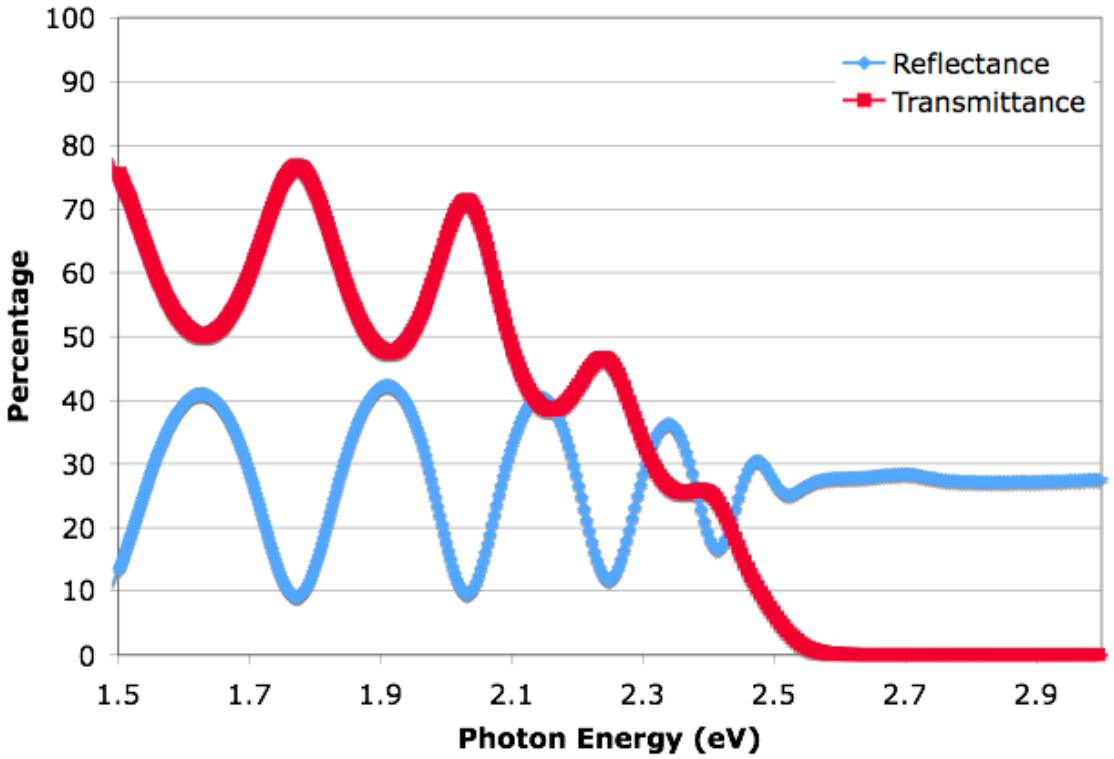

Figure 4-3: Percentage reflectance and transmittance of energy at different photon energies for our Cu2O samples.

Next, using the reflectance and transmittance from the above data and eq. (43), we plot the absorption coefficient as a function of photon energy in Fig. 4-4

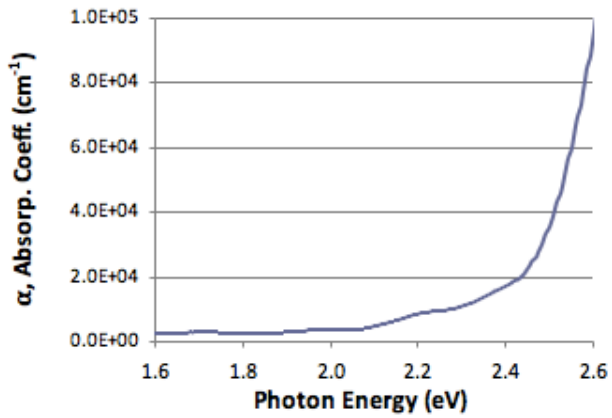

Figure 4-4: Calculated absorption coefficient as a function of photon energy.

It is unclear from inspection what form of band-edge transition is occurring in this sample, so it is necessary to fit the data to each transition model and determine which forms the best fit. For this sample, the exponent $m = {}^3/_2$ appears to form the best fit, indicating that at the band edge Cu_2O exhibits a forbidden direct transition. The fit reveals that the bandgap for this forbidden direct transition is approximately 1.93 eV as seen in Fig. 4-5:

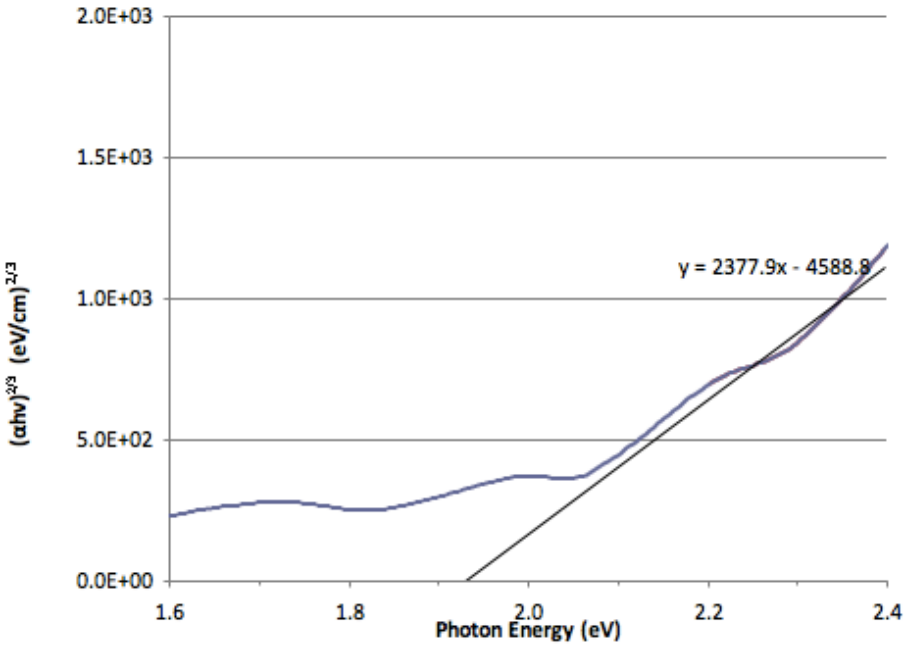

Figure 4-5: Absorption coefficient fitting to a forbidden direct transition.

Band-edge transitions in Cu_2O are in reality much more complicated, with several possible transitions available in a similar energy range to this forbidden direct gap. This is why the fit is accurate only over a small energy range and why the absorption coefficient grows immensely for photons beyond 2.4 eV.

Thus, we conclude that our film thickness is 268 nm and displays a forbidden direct bandgap of 1.93 eV. This thickness and absorption coefficient data will be useful later to inform our measurements of mobility and current output in the device.

4.3 Mobility Measurement

Initial mobility measurements performed on the present experimental setup characterized silicon wafers to within 5% of their known mobilities, proving that the setup can obtain both precise and accurate measurements of mobility.

The mobility measurement in the present work was conducted with a 600 nm thick Cu_2O sample deposited in a 1cmx1cm square at 350 ºC (623 K). Gold contacts 2mmx2mm were deposited in the four corners to interface with the chip holder described in Section 3.3.

First, Van der Pauw resistivity measurements were conducted. To avoid joule heating, small currents (5-50 nA) were used to probe the sample. At such small current values, the signal to noise ratio can be very small, requiring measurements to be taken over a longer period of time. Each current step of 5 nA was scanned for 3 seconds and the corresponding voltage difference was averaged and recorded. After confirming linearity, the voltage reading at 50 nA was saved and this data point was substituted into a Hall Effect spreadsheet for computation.

Due to the relatively low contact resistance, which is several orders of magnitude less than the resistance of the sample, contact resistance is assumed to be negligible. The

two x-direction and two y-direction resistances are averaged to give R_A and R_B respectively, and these values are used to solve for sheet resistance as in equation (50). Using an iterative solving process, the sheet resistance R_S is calculated to be 1.69E+6 Ω. Given the sample thickness of 600 nm, this results in a resistivity of 1.01E+2 Ω·cm.

For comparison, the resistivity of pure copper is 1.68E-6 Ω·cm while the resistivity of silicon is 6.4E+4 Ω·cm.

The next step is to calculate the Hall Effect mobility. Current was injected diagonally across the square sample (e.g. A to D) while voltage was measured across the opposite diagonal (B to C). All four diagonal directions were probed, using the same current ranges and sample times as the Van der Pauw measurement. All four measurements were performed separately at 0, +1.0, and -1.0 Tesla magnetic field strengths. Then, the four Hall coefficients defined in equation (52) were calculated and averaged to find a representative Hall coefficient for the sample. From this, the sample geometry, and the resistivity, we may compute the (unilluminated) majority carrier concentration and majority carrier mobility, which for p-type Cu_2O is holes.

From equations (53) and (54) the hole concentration is determined to be 1.1E+15 cm^{-3}, while the mobility is calculated to be 58.1 $cm^2/V{\cdot}s$.

As a brief check to determine whether or not these values are appropriate, we know from equation (28) that conductivity, and therefore resistivity is related to carrier concentration and mobility. The inverse of the product of carrier concentration, mobility, and resistivity should in fact equal q, the fundamental charge of a single carrier. Here, the inverse product equals 1.42E-19 C, which is very close with an error of -11.1%.

It is important to note that this is a measure of majority carrier mobility, not minority carrier mobility. Minority carrier mobility cannot be measured directly due to how few minority carriers are available relative to majority carriers. Yet, the relative masses of electrons and holes provide some clues. The effective mass of electrons $m_e^* = 0.99\ m_o$, and holes $m_h^* = 0.58\ m_o$ in Cu_2O suggests that the minority carriers, electrons, would have lower mobility due to their higher effective mass [25]. We expect minority carrier mobility to be proportional to majority carrier mobility by the same factor as the mass ratio between electrons and holes. As a result, the different masses would suggest a minority carrier mobility of approximately 34 $cm^2/V{\cdot}s$.

To examine the effect that this would have on diffusivity, we may calculate the diffusivity at room temperature using the Einstein equations (29). At a temperature of 300 K, these mobility values yield diffusivities of D_n = 0.88 cm^2/s and D_p =1.5 cm^2/s for electrons and holes respectively. Taking this one step further we may ask what carrier lifetime would be necessary to achieve a minority carrier diffusion length of 1 micron. With a minority carrier diffusivity of 0.88 cm^2/s, the diffusion length equation yields a necessary carrier lifetime of 1.14E-8 seconds. In other words, if carrier lifetime was at least 11 nanoseconds, given the electron mobility predicted in the current films, electrons could easily diffuse through the thickness of a thin-film solar cell.

Finally, compared to literature, the majority carrier mobility is quite high. The highest published mobilities are typically found in monocrystalline, oxidized samples, with mobilities of approximately 100 $cm^2/V{\cdot}s$ [26]. The fact that these polycrystalline sputtered films approach this mobility is proof of the quality of the films produced and represents a good sign that a production-friendly fabrication method does not have to compromise on quality.

4.4 Photoelectrochemical Cell Measurement

Unfortunately, the PEC cell measurements for Cu_2O encountered a number of challenges, preventing the collection of sufficient data. The sources of experimental difficulties will be discussed in this section, along with potential steps for overcoming these obstacles.

After the Cu_2O and decamethylcobaltocene junction was first assembled, the PEC cell was placed in the quantum efficiency measurement tool. A 100 W incandescent lamp was placed facing the cell to observe the photoresponse. Despite the strong light intensity, initially no photoresponse was observable. After consecutive reconfigurations and with still no photoresponse, the cell was disassembled, revealing a dark deposited circle on the Cu_2O film. This may have been the source of the lack of photoresponse, as chemicals from the electrolyte appeared to have deposited an insulative barrier on the surface. The first electrolyte batch had experienced several difficulties in mixing, and as a result the chemical composition may have been inappropriate.

A second batch of the decamethylcobaltocene electrolyte was mixed, this time taking care to add the chemicals in a specific order to ensure appropriate mixing. This time, a higher quality electrolyte was produced and initially resulted in a photoresponse under the 100 W lamp illumination. The monochromator single wavelength source appeared to have inadequate intensity to induce a photoresponse, so the I-V characteristic was conducted with the 100 W bulb.

However, upon performing a voltage sweep of 50 mV/s over the range -1.0 V to +1.0 V, the PEC cell no longer demonstrated a photoresponse. Attempts to recreate the initial photoresponse failed. Once again, the cell was disassembled, this time to find that the Cu_2O layer had been completely etched off to expose the gold underneath.

There are several possible explanations that may address the poor photoresponse and variability in solution performance. The first is that the chemicals were not purified properly, as suggested by the authors who initially proposed the use of decamethylcobaltocene redox pairs in Cu_2O applications [22]. Due to time and equipment limitations, several of the purification steps recommended were not conducted, perhaps resulting in an inferior electrolyte produced. Secondly, it is possible that the solution is highly sensitive to concentration or temperature. From cycling between the glove box, fume hood, and lab bench, the solution (despite being in a closed beaker for most of the time) could have experienced rapid temperature fluctuations or evaporation that may have changed the composition of the electrolyte. The enormous variation in result (deposition vs. etching) supports this theory of environmental variability. Finally, it is possible that at high enough applied voltages, unintended reactions are instigated, degrading the electrolyte or Cu_2O film in the process.

In the future, there are several possible steps for improving this particular measurement. The first step would be to purify the chemicals strictly as outlined in the literature [22], and re-attempt the same measurement with an improved electrolyte. Additionally, the applied voltages would be confined to ±500 mV to avoid unexpected electrochemical effects. The second option is to search for an alternative electrolyte with more simplicity to replace decamethylcobaltocene. This may be a viable option for ensuring higher repeatability in future measurements.

The final option for improving the measurement would be to find an alternative way to measure the same information. A p-n heterojunction with ZnO or ITO (indium tin

oxide) may provide an alternative material to form a junction and to explore the diffusion properties of Cu_2O. However, this introduces several new layers of complexity in modeling, fabrication, and junction engineering. Another alternative method is to focus on minority carrier lifetime instead. In tandem with mobility, carrier lifetime can actually provide an approximation for minority carrier diffusion length, rather than measuring it directly.

In summary, while the PEC cell diffusion length measurement would be a highly effective tool for rapidly characterizing the transport properties of films, it presented too many challenges to be of use in the present work. Regardless, the experimental methods were fully developed and will serve as a platform for eventually completing a successful measurement. It is the author's hope that the effort and lessons learned thus far will soon pay off in helping to achieve a successful reading

5. Conclusions and Next Steps

With every year of additional fossil fuel burned, the environmental damage continues to accumulate, bringing us closer to environmental tipping points particularly with regards to global climate change. To halt this progression, it is clear that carbon-free energy sources must become the dominant technologies of the 21st century. Yet, with such extraordinary energy consumption, it is not clear how we will meet increasing demand through sustainable means.

The surest path to dealing with the energy and climate crises long term is to identify energy sources that can provide a tremendous resource base for the foreseeable future without releasing atmospheric carbon. In addition, these sources must be scalable and cost-competitive with the fossil fuel technologies of the day. Solar appears to satisfy the first point, but has yet to prove itself scalable and inexpensive. To accomplish this, the advent of novel, earth-abundant materials as thin films will be necessary.

Yet, many of these materials still perform poorly in solar cell devices due to inferior material properties. While the focus of the present work is on Cu_2O in particular, this form of absorption and transport analysis could be applied to many other earth abundant materials in order to pursue improvements in the next decade.

In light of this utility, this thesis has aimed to establish a thorough and simple method for characterizing thin film solar cell materials by focusing on several critical material properties and developing appropriate measurement techniques for observing them. In particular, methods have been detailed that characterize the absorption, majority carrier mobility and concentration, and minority carrier diffusion length of a semiconducting film. Knowing these characteristics, while not a complete picture of the material, forms a very solid basis for predicting how eventual devices will perform and can identifying problems. Thus, these characterization methods can help photovoltaic researchers identify the material levers to pull in an effort to engineer better device performance.

Regarding Cu_2O in particular, the present work provides insufficient evidence for determining what the efficiency-limiting mechanisms are. The primary measurement of minority carrier diffusion length failed to yield significant results for Cu_2O specifically, perhaps due to incompletely purified electrolyte materials or due to adverse reactions occurring at the interface between the Cu_2O and electrolyte.

On other metrics, a strong picture of the reactively sputtered Cu_2O film performance emerged. The films exhibited strong absorptance, with an absorption coefficient in excess of 10^5 cm^{-1} for photons with energy exceeding 2.6 eV. In transport properties, the majority carrier mobility demonstrated that polycrystalline, sputtered films can approach the performance of monocrystalline films.

In addition to providing, strong, repeatable measurements, the mobility tools provided the opportunity to estimate the diffusivity of the material and additionally predict the necessary minority carrier lifetime required to achieve a high-performance device.

Given the high mobility and strong absorption of these films, the causes of poor performance remain unclear. The primary candidate is likely minority carrier lifetime. With a direct band transition and a high defect concentration, it is expected that recombination rates may be quite high. These high recombination rates may exist both in the bulk and at the surface, a particular form of recombination not entertained in the present work. An additional efficiency limiting mechanism could be the high exciton binding energy – despite photons readily absorbing at the band edge, they may only be forming excitons instead of separate electrons and holes, and excitons are much more difficult to separate.

Finally, the cause of low efficiencies may be due in large part to poor device engineering. As Cu_2O can only be fabricated as a p-type semiconductor and maintains such high electron affinity, it is very difficult to form a junction with it. Perhaps the material properties are sufficient; it may just require a clever integration of Cu_2O with an electrolyte, metal, or n-type heterojunction to see the device excel.

This discussion helps identify the next steps forward for research in this field. It is clear that some material properties have not been fully characterized yet, but the photoelectrochemical cell may not be the most efficient way to discover these material properties. In fact, a direct measurement of minority carrier lifetime may be a stronger option in the short term, as in tandem with mobility it may provide an approximate estimate of minority carrier diffusion length. In addition, opening dialogue with colleagues who have experience in PEC cells and in particular with decamethylcobaltocene may provide some insights to help diagnose the measurement problems and improve the results.

Finally, the most important next step is to begin the process of building Cu_2O devices. As the present work has demonstrated, building devices or junctions can actually serve as tools for analyzing basic material properties while simultaneously pushing the boundary of performance. This will require a change in priorities, but could in the long run yield benefits both for basic materials research and practical device implementation.

In conclusion, by working to understand the basic underlying mechanisms in a solar cell and developing robust ways of measuring them, we have set the stage for a more thorough model of Cu_2O thin film properties. Now, we have the opportunity to shape these properties to try to integrate earth abundant films into a working device. Every year that solar cells are delayed adds 30 billion tons of CO_2 to the atmosphere. That perspective just might be enough to inspire a breakthrough.

Bibliography

[1] Energy Information Administration. International Energy Outlook Highlights 2010. DOE/EIA-0484, 2010.

[2] Energy Information Administration. Annual Energy Outlook 2011. DOE/EIA-0383, 2010

[3] P. Lorenz, D. Pinner, and T. Seitz. The Economics of Solar Power. *McKinsey Quarterly – Sustainability & Resource Productivity Initiative*, June 2008.

[4] C. Wadia, A. P. Alivisatos, and D. M. Kammen. Materials Availability Expands the Opportunity for Large-Scale Photovoltaics Deployment. *Environmental Science & Technology*, 43:2072-2077, 2009.

[5] U.S. Geological Survey. Copper. *Mineral Commodity Summaries*, January 2011.

[6] F. L. Weichman. Photoconductivity of Cuprous Oxide in Relation to Its Other Semiconducting Properties. *Physical Review*, 117:998-1002, 1960.

[7] A. Mittiga, E. Salza, F. Sarto, M. Tucci, and R. Vasanthi. Heterojunction solar cell with 2% efficiency based on a Cu_2O substrate. *Applied Physics Letters*. 88:163502, 2006.

[8] W. Shockley and H. J. Queisser. Detailed Balance Limit of Efficiency of p-n Junction Solar Cells. *Journal of Applied Physics*, 32:510, 1961.

[9] S. A. Moskalenko. Appendix A: Properties of Excitons in Cu_2O, in *Bose-Einstein Condensation of Excitons and Biexcitons*. (Academy of Sciences of Moldova, 2010).

[10] R. W. O'Connell. Supplement II. *University of Virginia, Astronomy 121*. Retrieved May 6, 2011 from http://www.astro.virginia.edu/class/oconnell/astr121/guide10-s04.html

[11] National Renewable Energy Laboratory. Reference Solar Spectral Irradiance. *Renewable Resource Data Center*. Retrieved May 6, 2011 from http://rredc.nrel.gov/solar/spectra/am1.5/

[12] A. W. Bott. Electrochemistry of Semiconductors. *Current Separations*, 17:3, 1998.

[13] B. Madore. A Knowledgebase for Extragalactic Astronomy and Cosmology. *California Institute of Technology*. Retrieved May 6, 2011 from http://nedwww.ipac.caltech.edu/level5/Sept03/Li/Figures/figure8.jpg

[14] J. Bardeen, F. J. Blatt, and L. H. Hall. Indirect Transitions from the Valence to the Conduction Bands, in *Proceedings of the Conference on Photoconductivity*, Atlantic City, 1954 (J. Wiley & Sons, Inc., New York, 1956), p. 146.

[15] S. R. Wenham, M. A. Green, and M. E. Watt. Applied Photovoltaics. (Centre for Photovoltaic Devices and Systems, UNSW, 2007).

[16] C. Honsberg and S. Bowden. PVDCROM. *pveducation.org*, 2010. Retrieved May 6, 2011 from http://pveducation.org/pvcdrom

[17] W. Gärtner. Depletion-Layer Photoeffects in Semiconductors. *Physical Review*, 116:84-87, 1959.

[18] B. A. Movchan and A. V. Demchish. *Physical of Metals and Metallography*, 28:83, 1969.

[19] B. van Zeghbroeck. Principles of Semiconductor Devices. *University of Colorado*, 2007. Retrieved May 6, 2011 from http://ecee.colorado.edu/~bart/book/book/chapter2/pdf/ch2_7_5.pdf?q=2the

[20] W. R. Thurber. Hall Effect Measurements. *National Institute of Science and Technology*. Retrieved May 6, 2011, from http://www.nist.gov/pml/semiconductor/hall.cfm

[21] P.A. Verlangieri , M. Kuznetsov, and M.V. Schneider. Low resistance ohmic contacts for microwave and lightwave devices. *IEEE Microwave and Guided Wave Letters*, vol.1 no.3, 1991.

[22] C. Xiang, N. S. Lewis, et al. 820 mV open-circuit voltages from Cu_2O/CH_3CN junctions. *Energy and Environmental Science*, 4:1311-1318, 2011.

[23] V. D. Das and L. Damodare. Photoelectrochemical investigations on n-$CdSe_{0.5}Te_{0.5}$ thin-film electrode/polyiodide system. *Materials Chemistry and Physics*,56:116-124, 1998.

[24] Y. S. Lee, M. T. Winkler, S. C. Siah, R. Brandt, and T. Buonassisi. Hall mobility of cuprous oxide thin films deposited by reactive direct-current magnetron sputtering. *Applied Physics Letters*, Accepted April 20, 2011.

[25] W. Y. Chang, Y. N. Xu, and K. W. Wong. Ground-state and optical properties of Cu_2O and CuO crystals. *Physical Review*, B 40:7684–7695, 1989.

[26] H. Matsumura, A. Fujii, and T. Kitatani. Properties of High-Mobility Cu_2O Films Prepared by Thermal Oxidation of Cu at Low Temperatures. *Japanese Journal of Applied Physics*, 35:5631-5636, 1996.